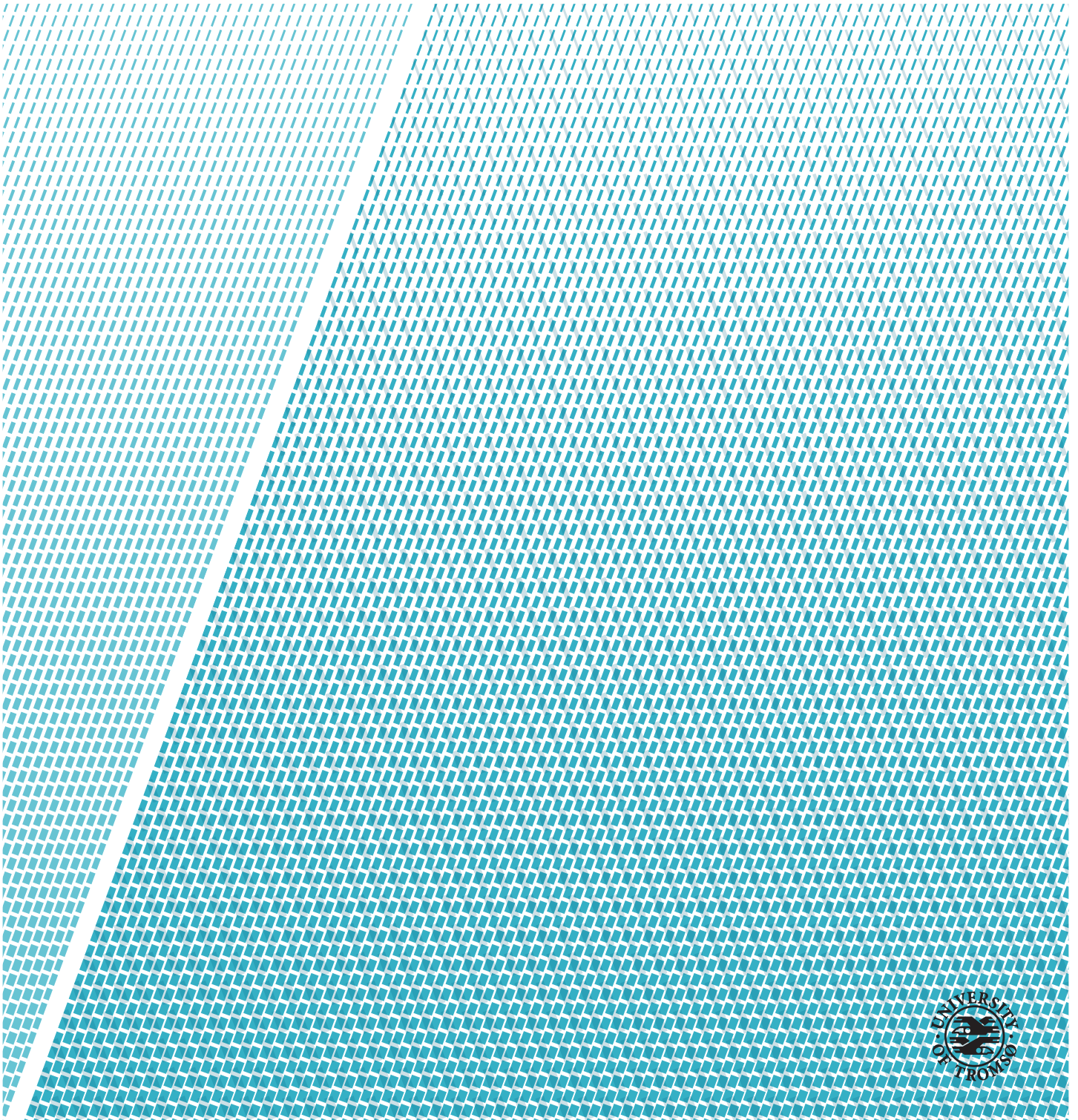


Laser Based Altimetry for Unmanned Aerial Vehicle Hovering Over a Snow Surface

Hallvard Haugen

FYS-3941 Masters Thesis in Applied Physics and Mathematics



Abstract

A microwave radar for non-invasive snow stratigraphy measurements has been developed. Results were promising, but it failed to detect light powder snow in the air-snowpack interface. The aim of this thesis is to find and verify a system for estimating altitude on centimeter scale over a snow surface, independent of snow conditions. Also, relative pitch and roll angle estimation between the UAV and local surface should be resolved, to help directing the radar beam perpendicularly to the surface. After a variety of technical solutions were examined, we propose a system of three time-of-flight near-infrared altimeters pointing at different directions towards the surface. Experimental results showed RMS error of 1.39 cm for range estimation averaged over the most common snow types, and 2.81 cm for wet snow, which was the least reflective medium. An experiment conducted for an array of two altimeters scanning over a snow surface, showed that the local, relative surface tilt was found to be accurate within $\pm 2^\circ$ given that it was sufficiently planar. Further, the altitude RMS error was estimated to 1.57 cm. We conclude that the chosen altimeter was within the requirements, and that an array of three altimeters would give acceptable relative tilt estimation in to planes on the snow surface. The system should be subject to flight testing and implemented on UAV platform such that it can aid the microwave radar system during snow scanning.

Acknowledgements

Fyrst og fremst vil eg takke professor Svein Jacobsen for hjelp og rettleiing utover det ein kan vente seg i arbeidet med oppgåva. Svein sitt engasjement og tru på prosjektet har vore til stor inspirasjon.

Eg vil og takke mine gode vener Sara Björk og Torgeir Blæsterdalen for å ha lært meg eit og anna om akademisk skriving, og for omfattande hjelp i innspurten. Eg vil og takke Rolf Ole Rydeng Jenssen for inspirerende diskusjonar.

Til slutt vil eg takke kontorgjengen for å ha gjort det siste året såpass bra som det har vore. Ikkje minst må velferdsansvarleg Trond-Ola takkast for namneskilt, julepynt og store mengder sukker- og koffeinfri energidrikk. Eg vil og rette ei takk til Brynjulv Tveit for godt samarbeid i fem år, og til Trine for å ha holdt meg i live dei siste månadane med graut og kaffi.

*Hallvard Haugen
Tromsø, Juni 2017*

Contents

Abstract	i
Acknowledgements	iii
List of Figures	ix
List of Tables	xi
My list of definitions	xiii
Nomenclature	xv
1 Introduction	1
1.1 Aim of Study	3
1.2 Related Studies	3
1.3 Structure of Thesis	4
I Background Theory	7
2 Scattering Theory	9
2.1 Characteristics of a Random Rough Surface	10
2.1.1 Spatial Autocorrelation	10
2.1.2 Rayleigh Roughness Criterion	11
2.2 Electromagnetic Theory	12
2.2.1 Boundary Conditions	13
2.3 Fresnel Equation	14
2.3.1 Lossy Media	15
2.4 Bidirectional Reflectance Distribution Function	16
2.5 Green Functions	17
2.6 Random Rough Surface Scattering models	18
2.7 Internal Scattering	18
3 Altimetry	21

3.1	GPS and Barometer Based Altimetry	21
3.2	Rangefinders	22
3.2.1	Time of Flight	22
3.2.2	Frequency Modulated Continuous Wave	22
3.2.3	Optical Triangulation	23
3.2.4	Ultrasonic Rangefinders	23
3.3	Systems for Target Localization	24
3.3.1	Simultaneous Localization and Mapping	24
3.3.2	Array of TOF Sensors	25
4	Classification of Seasonal Snow and its Optical Properties	29
4.1	Metamorphism of Snow	30
4.1.1	Dry Metamorphism	30
4.1.2	Wet Metamorphism	31
4.1.3	Temperature Gradient Metamorphism	31
4.2	Optical Properties	32
4.2.1	Optical Equivalent Grain Size	33
4.2.2	Geometrical Surface Characterization	35
4.2.3	Bidirectional Reflectance Distribution Function	36
4.2.4	Optical Attenuation in Free Space	37
4.3	Avalanches	39
5	Choice of Altimetric System	41
5.1	Decisive Factors	42
5.1.1	Accuracy and Range	42
5.1.2	Scattering and Reflectivity	42
5.1.3	Beam Divergence	43
5.1.4	Physical Size and Power Consumption	44
5.2	Discussion	44
II	System Description and Implementation	47
6	SF10 Lightware Rangefinder	49
6.1	Signal Sampling	50
6.2	Noise	51
6.3	Interfacing by Lightware Terminal	53
6.3.1	Hacking the SF10	53
6.4	Case Study: Range Measurements	54
6.4.1	Results	55
6.5	Case Study: Signal Strength Measurements	57
6.5.1	Results	58
6.6	Safety	60

7	Experimental Setup	63
7.1	Goals of Experiments	63
7.2	Stationary Experiment	64
7.3	Scanning Experiment	64
7.4	Altitude Estimation by Camera	65
7.4.1	Edge detection	66
7.4.2	Image Smoothing	66
7.4.3	Model Physical Altitude from Image	66
7.4.4	Digital Camera	67
7.4.5	Altitude Estimation by Camera Algorithm	67
7.4.6	Parameters	68
8	<i>In situ</i> measurements	71
8.1	Grain Size and Shape	71
8.2	Hardness	72
8.3	Temperature and Humidity	72
III	Results	75
9	Stationary Experiment	77
9.1	Snow Conditions	78
9.2	Results	79
10	Scanning Experiment	83
10.1	Array	86
11	Complementary Results	89
11.1	Long Ranges	89
11.2	Crosstalk	91
IV		93
12	Suggestion to Implementation of Array Setup	95
12.1	Physical Setup	95
12.2	Implementaion to the UAV Control System	97
13	Discussion	99
13.1	Stationary Experiment	99
13.2	Scanning Experiment	101
13.3	Complementary Results	102
13.4	Choice of Altimetric System	103
13.4.1	Lidar	103

13.4.2 Radar Rangefinders	103
13.4.3 Acoustic Rangefinder	104
13.4.4 Laser Rangefinder	104
14 Conclusions	107
14.1 Future Work	108
Bibliography	109

List of Figures

2.1	Phase variations due to roughness and incident angle	11
2.2	Incident EM wave onto a boundary	13
2.3	Fresnel reflection on air to snow	15
2.4	Presentation of the geometrical nomenclature in BRDF . . .	16
2.5	Diffuse vs specular reflection pattern	17
3.1	Concept of optical triangulation	23
3.2	Principle sketch for an array of two TOF sensors	26
4.1	The relation between melting temperature and grain size . .	31
4.2	Photo of surface hoar	32
4.3	Real and Imaginary refractive index of ice	33
4.4	Reflection coefficient versus wavelength for snow	34
4.5	Modeling non-spherical grains as spheres	35
4.6	Simplified BRDF for optical radiation onto a snow surface . .	37
4.7	Optical attenuation of 905 nm wave propagation in free space	39
6.1	The SF10 rangefinder	49
6.2	Principle of sequential equivalent time sampling	51
6.3	Dynamic power range of a sensor system	52
6.4	Lightware Terminal live output sensor data.	53
6.5	Thresholding algorithm applied on real SF10 data	56
6.6	Error of the measurements at various distances	57
6.7	Experimental setup for signal strength measurements	58
6.8	Integrated signals at various angles	59
6.9	Comparison of SS and integrated pulses	59
6.10	Absolute error versus normalized signal strength	60
6.11	Sticker on the SF10 claiming its safety classification	61
7.1	Setup for stationary experiment	65
7.2	Scanning experiment setup and example picture frame	69
8.1	Magnifying loupe and crystal study card	72

9.1	Melt forms collected January 27	78
9.2	Precipitation particles and large surface hoar crystals	79
9.3	Signal strength during stationary experiment	81
9.4	Error in range measurements during the stationary experiment	82
10.1	Cross section of the snow pit	84
10.2	Comparison of AEC and SF10 height data	85
10.3	Error of SF10 altimeter data compared to AEC data.	85
10.4	Data obtained by array setup	86
10.5	Height data from array setup	87
10.6	Surface angle obtained by array setup	88
11.1	Setup when applying the SF10 on long ranges	89
11.2	Error and SS at long ranges	90
11.3	Setup for crosstalk experiment	91
12.1	2D versions of the array setup	97
12.2	3D versions of the array setup	97
12.3	Pixhawk UAV control board gimbal	98
13.1	Array setup on surface with roughness on two scales	101

List of Tables

3.1	Nomenclature of the array of two rangefinders	25
4.1	Classification of seasonal snow	30
4.2	Classification of grain size	30
5.1	List of typical high accuracy altimeters	41
5.2	Comparison of altimeters in regards to accuracy and range .	42
5.3	Comparison of the altimeters due to its scattering characteristics	43
5.4	Comparison of beam divergences of the given altimeters. . .	44
5.5	Comparison of altimeters size, weight and power consumption	44
6.1	Specifications for the Lightware SF10	50
7.1	Features of the stationary experiment	64
7.2	Features of the scanning experiment	65
7.3	Specifications for camera applied for surface mapping	67
8.1	<i>In situ</i> measurements of hardness of snow	72
9.1	Overview of snow conditions	78
9.2	RMS error of the measurements on snow	82
10.1	Comparison of AEC data with SF10 data	85
10.2	Estimated surface tilt	88
11.1	Results from crosstalk experiment	91

My list of definitions

ACF	Autocorrelation Function
AEC	Altitude Estimation by Camera
ASL	Above Snow Level
BRDF	Bidirectional Reflectance Distribution Function
EM	Electromagnetic
FSO	Free Space Optics
GPS	Global Positioning System
IR	Infrared
LT	Lightware Terminal
NIR	Near-Infrared
RF	Radio Frequency
RMS	Root Mean Square
RPAS	Remote Operated Aerial Systems
SETS	Sequential Time Equivalent Sampling
SLAM	Simultaneous Localization and Mapping
SS	Signal Strength
UAV	Unmanned Aerial Vehicle
UV	Ultraviolet
UWB	Ultra Wide Band
UWiBaSS	Ultra Wide-Band Snow Sounder

Nomenclature

In this thesis, mathematical operators are in upright letters and symbols in italics. The list below presents a selection of the symbols used.

E Electric field component of EM wave [Vm^{-1}]

f Frequency [Hz]

h Altitude [m]

i Imaginary unit [$\sqrt{-1}$]

I Image function

k Wavenumber [m^{-1}]

l_a Absorption length [m]

l_c Correlation length [m]

n Refractive index

R_a Rayleigh roughness parameter

s Distance between illuminated spots on the ground [m]

ϵ Absolute permittivity of medium

ϵ_r Relative permittivity of medium

ζ Surface height [m]

θ Incident angle [rad]

λ Wavelength [m]

μ Permeability of medium

σ_h Surface height standard deviation [m]

ϕ Surface tilt angle [rad]



Introduction

Snow and ice cover about one sixth of the Earth's surface [54] and can appear as seasonal snow, glaciers or sea ice. These media have been studied for a variety of reasons, over a long period of time. Due to the high albedo of snow, it has a vital impact on the global energy balance, and thus mapping the snow cover extent is of interest in the field of climatology [72, 29]. Further, the albedo of snow can fall from 90 to 50% as snow ages, and thus specific knowledge of the snow conditions have importance in climate models [73]. Hydrological run-off models, which are used in prediction of floods and forecasting hydropower production, also benefit from surveying snow conditions [61]. Remote sensing systems have a huge potential in estimating snow depth and snow water equivalent, which describes the potential run-off from a terrestrial snow [11, 57].

Avalanches are the main natural hazard in snow covered areas, damaging infrastructure and annually taking around 250 lives worldwide [67]. For those reasons, and by the fact that back-country ski touring and population in potentially hazardous areas are increasing, avalanches are currently an active field of research [67]. Traditionally, avalanche observation techniques were limited to *in situ* measurements, conducted by trained professionals digging snow pits, probing, etc. However, avalanche starting zones are located in steep ($>30^\circ$ [70]), remote and possibly dangerous areas, which makes gathering of data a rare event [64]. In order to provide data with temporal reliability and large spatial coverage, the use of remote sensing systems have been included in the avalanche research. Remote sensing is the science of measuring a phenom-

ena without being in direct contact¹, and can be implemented in spaceborne, airborne and ground-based platforms. Studies by Buhler [8] and Eckerstorfer et al [17] state that remote sensing has a large potential in estimating parameters like snow depth, snow type and detect recent avalanche activity. Layering of the snowpack, which is the single most important factor in forecasting dangerous, slab avalanches [70, 38], can be described by ground penetrating radar [17]. Persistent weak interfaces between slabs in the snow pack, can appear due to certain accumulation and metamorphic processes in the snowpack [70, 38]. They will appear as layers of some centimeters of large, faceted crystals with low density, and thus ground penetrating radars require correspondingly high longitudinal resolution to resolve information about these layers. Acceptable along-beam resolution can be provided by ultra wide-band microwave (MW) radars [13]. Considering that wide-banded signals are expensive to amplify, and that the signal reduces to the fourth power of range due to spreading loss [52], measurements performed at low altitudes are preferred. Thus, unmanned aerial vehicles (UAV) may be the ideal platform to carry the radar.

To bridge the gap between more expensive spaceborne and manned airborne platforms and *in situ* measurements on ground, UAVs can be applied. UAVs or remote operated aerial systems (RPAS), have become increasingly popular in both military, research and commercial applications. Recent technology advances have made UAVs significantly more effective and less expensive, not least because of the miniaturization of sensors and electronics. As such components have become smaller, lighter and less expensive, they are possible to integrate on a free-standing platform like an UAV [43].

UiT the Arctic University of Norway together with NORUT IT have developed the Ultra Wide-Band Snow Sounder (UWiBaSS), a light medium penetrating radar aiming to describe the vertical layer distribution of the snow pack. The UWiBaSS was designed such that it is a feasible payload on a UAV, which enables the radar to scan the snow at low altitudes. Data collected can be used in avalanche forecasting, but it may also benefit other snow survey purposes. The UWiBaSS is an ultra wide band microwave (MW) radar with operational bandwidth from 0.1-6 GHz. Maximum range is given to 5.9 m with a range resolution of 5.3 cm [26]. Results from experimental work of Jenssen [26] showed that the radar detected the most prominent vertical transitions in the snow with an RMS error of 2.48 cm. However, due to the high fractional air content of dry powder snow, the snow-air interface seemed invisible in the UWiBaSS frequency spectrum. This was a serious drawback, as the snow surface is an important reference interface in the pulse deconvolution process. Hence, the main motivation behind this thesis is to develop an alternative system capable of detecting snow with low dielectric constant.

1. http://glossary.ametsoc.org/wiki/Remote_sensing

1.1 Aim of Study

This thesis aims to find and verify an altimetric system that, regardless of snow conditions, can estimate the distance to the snow surface with an accuracy that is better than the UWiBaSS range resolution of 5.3 cm, as this is expected to be improved in the future.

To achieve this, we will look into altimetric concepts that have the required accuracy, and that utilizes electromagnetic radiation in the millimeter and optical band as well as acoustic waves. First, we will study their reflective and scattering properties, and based on that choose an altimeter suited for the purpose. Then we will design and conduct experiments with the goal of verifying that the altimeter will estimate distance to the snow surface within the required accuracy for ranges, angles and snow types that is likely to appear when applying an UAV as platform for the UWiBaSS.

Generally, backscattering of microwave radiation onto a snow surface depends highly on the incident angle [54]. Hence, the radar beam should be directed perpendicularly to the snow surface in order to ensure sufficient intensity of the received signal. We therefore want to use the chosen altimeter to determine the relative angle between the radar and the snow surface. This should also be verified experimentally. The relative angle can be utilized as input in the UAV control system and help ensuring the radar to be correctly oriented in real time.

To sum up, the aim of this thesis is to find and verify a system that

- Finds range to snow surface with error less than 5.3 cm.
- Resolve relative angle to the local snow surface.
- Has acceptable size, weight, energy consumption and computational demands, such that it is feasible as payload on a small UAV.

1.2 Related Studies

Altimetry with centimeter scale resolution is mostly studied in relation to autonomous takeoff and landing UAVs. A study by Cho et. al [12] showed that by including a frequency modulated continuous wave (FMCW) radar altimeter, height resolution was improved to 2 cm. The study expresses concern of the robustness of the radar altimeter, and by sensor fusion they include gyro and GPS for more stable altitude estimations. This was a general article, not

focusing on hovering over a snow surface.

Similar to the problem of determining accurate altitude of an UAV, there are studies that consider automatic measurements of the snowpack depth by stationary ground-based or airborne sensors. A downward facing sensor is recording the distance to the surface as snow accumulates and melts during the winter. By comparison to the known ground level, the snow depth can be found. Ayan et. al [5] applied a millimeter wave FMCW radar in ground-based snow measurements. The results were promising, with sub-centimeter resolution and signal sustained at moderate deviations in incident angle, but it was emphasized that it required testing on snow types that not had been present during the measurement campaign. A laser rangefinder was used as reference (true value), but it was expressed concerns that atmospheric disturbance like precipitation or fog could have influence on the laser signal. Deems et. al [14] presents a review article on how either airborne or ground-based rotating laser rangefinders, referred to as lidars (light detection and ranging), can be applied for snow depth mapping. The study indicates that visible and near-infrared (NIR) scanning have promising potential in snow depth mapping, and that ground-based lidar can reach accuracy on millimeter level.

1.3 Structure of Thesis

The thesis is divided into four parts:

Part I presents the background theory. Chapter 2 contains scattering theory, including fundamental electromagnetic theory, characterization of rough surfaces and models for describing scattering and reflection. Chapter 3 starts out with introducing conventional altimetric systems and ends up with more sophisticated approaches, resolving both altitude and attitude. In chapter 4, a brief introduction on metamorphism of snow make the grounds for discussing its optical properties. Based on the previous chapters, we compare different altimeters in chapter 5, and the discussion ends with choosing the NIR altimeter.

Part II describes the system and how the experiments are conducted. In chapter 6, the chosen altimeter is described by its specifications, and some experiments performed to increase the knowledge of the sensors are presented. Chapter 7 describes thoroughly how experiments are conducted and chapter 8 present *in situ* measurements tools and methods.

Part III presents the results of the main measurements campaigns, which are the stationary, scanning and complementary experiments. It includes correla-

tion with reference data.

Part IV first presents a possible implementation of the proposed altimetric system in chapter 12. In chapter 13 we discuss the validity of the obtained results, the correlation with the reference data and how promising the altimetric system is compared to other possible solutions. In chapter 14 we draw the main conclusions, and discuss possible future work.

Part I

Background Theory

/2

Scattering Theory

When electromagnetic (EM) radiation impinges a surface, it is either reflected, transmitted or absorbed through this interface. By the law of energy conservation, the sum of reflected, transmitted or absorbed energy is equal to the energy of the incident wave. In this chapter, we will look into what factors that determine how the energy is distributed between the mentioned components. However, the main body of the chapter will cover the theory of scattering. A scattered wave is defined by the International Institute of Electrical and Electronics Engineering (IEEE) as: "An electromagnetic wave that results when an incident wave encounters the following:

1. One or more discrete scattering objects
2. A rough boundary between two media
3. Continuous irregularities in the complex constitutive parameters of a medium" [1]

According to number 2, an EM wave hitting a surface will provide a scattered field if the surface is defined as rough. To determine if a surface is rough in an electromagnetic sense, both topography and wavelength must be considered. This will be introduced early in this chapter. Snow is a porous medium consisting of ice and air, and for wet snow, also free liquid water. Thus, throughout the snow pack, radiation transmitted through the surface, may encounter numerous air, ice and water interfaces that can induce internal scattering [54],

according to number 3. An introduction on internal scattering will be given late in this chapter.

2.1 Characteristics of a Random Rough Surface

The reflected wave from a snow surface is not only dependent on the relative properties the media, snow and air, and incident angle, but also the topographic height variations of the surface. The snow surface is a complex rough surface, and must be described by its statistics. To describe the height distribution, three parameters are needed [51]

- mean surface height ζ_0
- surface height standard deviation σ_h
- distribution; could be Gaussian, Exponential, Lorentzian, etc.

If the the surface is assumed Gaussian, the height distribution p_h is given:

$$p_h(\zeta) = \frac{1}{\sigma_h \sqrt{2\pi}} \exp \left[-\frac{1}{2} \left(\frac{\zeta - \zeta_0}{\sigma_h} \right)^2 \right], \quad (2.1)$$

where ζ denotes the surface height. For simplicity the average (mean) of the surface height is set to be zero. The centered second order moment (variance) is given:

$$\langle \zeta^2 \rangle = \int_{-\infty}^{\infty} \zeta^2 p_h(\zeta) d\zeta = \sigma_h^2 \quad (2.2)$$

also known as the RMS height. The $\langle \cdot \rangle$ is equivalent to the expectation operator $E\{\cdot\}$.

2.1.1 Spatial Autocorrelation

The correlation of the surface height between two points on the horizontal axis r_1 and r_2 is given by its autocorrelation function (ACF). A periodic surface will have a periodic ACF. In general the AFC is given by:

$$W_h(r_1, r_2) = \langle \zeta(r_1) \zeta(r_2) \rangle. \quad (2.3)$$

The autocorrelation coefficient $C_h(r_d)$ is a normalized version of the ACF. For a wide-sense stationary surface (WSS) [21] the ACF simplifies to

$$C_h(r_d) = \frac{\langle \zeta(r_1)\zeta(r_1 + r_d) \rangle}{\sigma_h^2} \quad (2.4)$$

where $r_d = r_1 - r_2$. Thus, the correlation is only dependent of their relative horizontal distance and not their absolute position, as in the general definition. The WSS assumption makes it possible to define a correlation length l_c general for one horizontal axis. The correlation length gives a measure of the scale of roughness. It is defined as $l_c = r_d$ when $C_h(r_d) = 1/e$. From the assumption of WSS the frequency spectrum of the surface can be obtained by a Fourier transform of the ACF [21].

$$S_h(k) = \text{FT}[W_h(r_d)] = \int_{-\infty}^{\infty} W_h(r_d)\exp(-ik \cdot r_d)dr_d \quad (2.5)$$

where k is the wavenumber of the surface height. There are several other statistical parameters to describe a rough surfaces [51], most important amongst them is the RMS slope given by:

$$\sigma_s = \sqrt{\langle [\zeta'(x) - \langle \zeta'(x) \rangle]^2 \rangle}, \quad (2.6)$$

where $\zeta'(x)$ denotes the derivative of the surface height.

2.1.2 Rayleigh Roughness Criterion

The electromagnetic roughness of a surface is in addition to its topography given by the wavelength and angle of the incident EM radiation. These factors will determine the phase variations between incident and reflected waves and further will the phase considerations define how constructive and destructive interference will affect the reflected field.

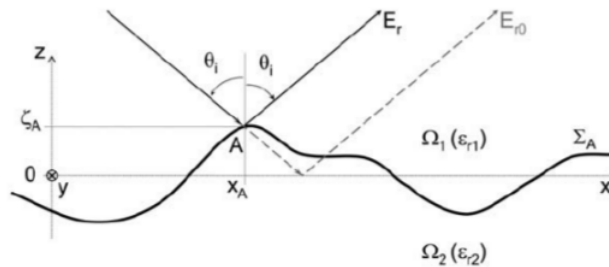


Figure 2.1: Phase variations due to roughness and incident angle of a plane EM wave E_r . Reprint from [51]

In figure 2.1, E_{r0} is the average reflected field and E_r is the reflected wave from point A. $\Omega(r)$ denotes the properties of the media. The phase variation $\delta\phi_r$ between E_{r0} and E_r is given by:

$$\delta\phi_r = 2k_1\zeta_A\cos\theta_i, \quad (2.7)$$

where k_1 is the wavenumber in the upper region and ζ_A is the vertical distance from $\langle\zeta\rangle$ to point A. To distinguish between different surfaces, the Rayleigh roughness parameter R_a is defined:

$$R_a = k_1\sigma_h\cos\theta_i. \quad (2.8)$$

In general, for smooth surfaces R_a will be small, and for large rough surfaces R_a will be large. The exact limits for R_a used in classifying a surface as smooth, rough or very rough surface is not consistent in the literature. Though, it is clear from eq. (2.7) that the reflected waves propagate in a constructive manner if:

$$R_a < \frac{\pi}{4}, \quad (2.9)$$

the surface is classified as slightly rough according to Pinel and Bourlier [51]. As R_a increases over the $\pi/4$ -limit, the coherent component of the reflected wave vanishes compared to the incoherent, and the scattering becomes diffuse. For $k_1 = 2\pi/\lambda_1$ equation (2.8) and (2.9) reduces to:

$$\sigma_h < \frac{\lambda_1}{8\cos\theta_i}. \quad (2.10)$$

From eq. (2.10) it is easy to see that if the surface height standard deviation is less than 1/8 of the wavelength for normal incident wave, the surface can be assumed slightly rough. For increasing incident angle, the height standard deviation needs to be less to give this conclusion.

2.2 Electromagnetic Theory

A complete description of the electromagnetic field is provided by the famous Maxwells Equations, assumed linear, homogeneous and isotropic media (LHI), can be given by:

$$\nabla \times \mathbf{H} - \frac{\partial \mathbf{D}}{\partial t} = \mathbf{J} \quad (2.11)$$

$$\nabla \times \mathbf{E} + \frac{\partial \mathbf{B}}{\partial t} = \mathbf{0} \quad (2.12)$$

$$\nabla \cdot \mathbf{D} = \rho \quad (2.13)$$

$$\nabla \cdot \mathbf{B} = \mathbf{0} \quad (2.14)$$

where \mathbf{E} and \mathbf{H} denotes the electric and magnetic field, and \mathbf{D} and \mathbf{B} the electric displacement and magnetic induction. \mathbf{J} is the electric current density and ρ the electric charge density. The quantities above are related:

$$\mathbf{D} = \epsilon \mathbf{E} = \epsilon_0 \epsilon_r \mathbf{E} \quad (2.15)$$

$$\mathbf{B} = \mu \mathbf{H} = \mu_0 \mu_r \mathbf{H} \quad (2.16)$$

$$\mathbf{j} = \sigma \mathbf{E}. \quad (2.17)$$

From equation (2.11) and (2.12) one can derive the inhomogeneous Helmholtz equation:

$$\nabla \times \nabla \mathbf{E} - k^2 \mathbf{E} = i\omega \mu \mathbf{J}, \quad (2.18)$$

where k is squared wave number $k^2 = \omega^2 \mu \epsilon$

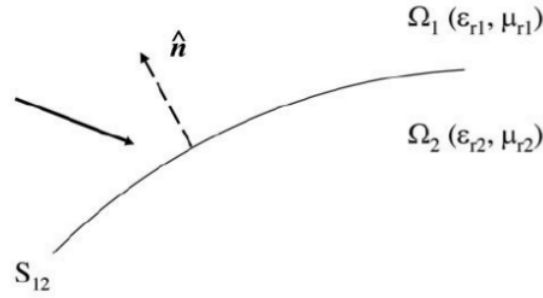


Figure 2.2: Incident wave on a surface S_{12} that represent the boundary between the linear, homogeneous, isotropic media (LHI) Ω_1 and Ω_2 . Reprint from [51, p 4]

2.2.1 Boundary Conditions

The electromagnetic field across a surface interface as in figure 2.2 will satisfy the continuity conditions given in equation (2.19)-(2.22)

$$\hat{n} \times (\mathbf{E}_1 - \mathbf{E}_2) = \mathbf{0} \quad (2.19)$$

Thus, the tangential component of \mathbf{E} is continuous through the surface S_{12} . \hat{n} is the unit normal vector of the surface point into region 1.

$$(\mathbf{D}_2 - \mathbf{D}_1) \cdot \hat{n} = \rho_s \quad (2.20)$$

states if there is a non-zero surface charge ρ_s on S_{12} , the normal component of \mathbf{D} has a step at the surface equal to ρ_s . From

$$(\mathbf{B}_2 - \mathbf{B}_1) \cdot \hat{n} = \mathbf{0} \quad (2.21)$$

it is seen that the normal component of \mathbf{B} is continuous across S_{12} . Furthermore, for

$$\hat{n} \times (\mathbf{H}_2 - \mathbf{H}_1) = \mathbf{j}_s, \quad (2.22)$$

the tangential component of \mathbf{H} has a step equal to the surface current density \mathbf{j}_s at the surface.

2.3 Fresnel Equation

When electromagnetic radiation reaches a boundary, it is transmitted, reflected or absorbed. Maxwell equations and boundary conditions can be derived into Fresnel equations for reflectance and transmittance. However, they only hold for planar surfaces, with no internal scattering. The permittivity ϵ describes how electric fields are affected by a given medium. In the case of snow scattering, it is common to assume the affected media to be non-magnetic. A quantitative measure to what degree a given incident wave will be reflected can be provided by Fresnel's reflection coefficient, which for normal incident radiation can be stated [63]:

$$R = \left| \frac{n_1 - n_2}{n_1 + n_2} \right|^2. \quad (2.23)$$

n is the refractive index

$$n = c/v, \quad (2.24)$$

where c is the speed of light in vacuum, and v is the speed of light in the given medium. Hence, it is alternatively given by:

$$n = \sqrt{\epsilon_r \mu_r} \quad (2.25)$$

ϵ_r is the relative permittivity of the medium, and μ_r is permeability. For nonmagnetic media, $\mu_r = 1$, hence only ϵ_r will affect the refractive index. For lossless media ϵ_r is strictly real, and for light, dry snow it is near one, due to its high fractional air content. It is typically around 1.3-1.4 [23] at 10 GHz, but might be even lower. Figure 2.3 is derived from eq. (2.23) and (2.24) and shows that for dry snow in the microwave and millimeter wave spectrum, the reflection coefficient is low.

The return loss in decibels for snow with $\epsilon_r = 1.3$

$$RL = -20 \log_{10} |R| = -47.4 \text{ dB} \quad (2.26)$$

which is a significant loss. We assume surface to be flat in the electromagnetic sense, thus reflection to be specular, for which is not the case for a rough surface. Permittivity is generally a complex value, as absorption is taken into account.

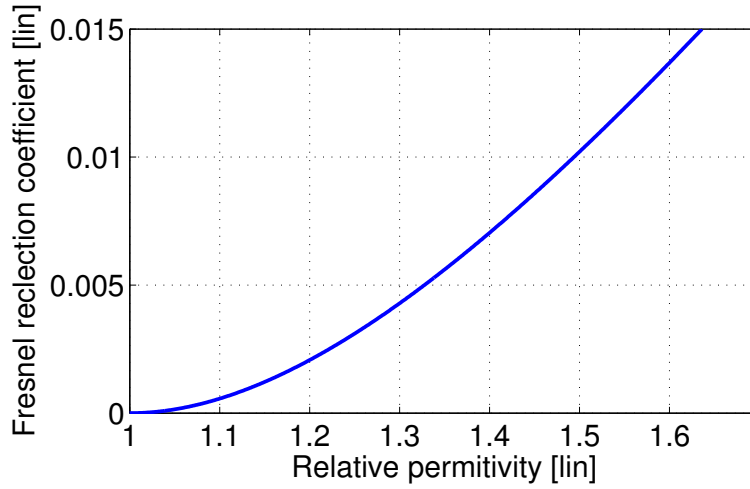


Figure 2.3: Fresnel reflection coefficient as a function of the permittivity of the surface medium relative to the incident medium.

2.3.1 Lossy Media

The permittivity for lossy homogeneous media is complex and given as:

$$\epsilon_r = \epsilon' - i\epsilon'' \quad (2.27)$$

where i is the imaginary unit defined $i^2 = -1$. ϵ' and ϵ'' are the real and the imaginary part of the permittivity. The refractive index n is in general also complex, and can be given

$$n = m - i\kappa \quad (2.28)$$

Still assuming $\mu = 1$, it follows from equation (2.25) that $\epsilon_r = n^2$ and by that the relation to permittivity can be found to be [55]:

$$\epsilon' = m^2 - \kappa^2 \quad (2.29)$$

$$\epsilon'' = 2m\kappa \quad (2.30)$$

Applying the complex refractive index on a plane wave the interesting quantity absorption length l_a can be derived [55]:

$$l_a = \frac{c}{2\omega\kappa}, \quad (2.31)$$

which is defined as the distance a wave can propagate until the flux density is reduced by a factor of e . It implies that the attenuation is determined by the imaginary part of the refractive index κ .

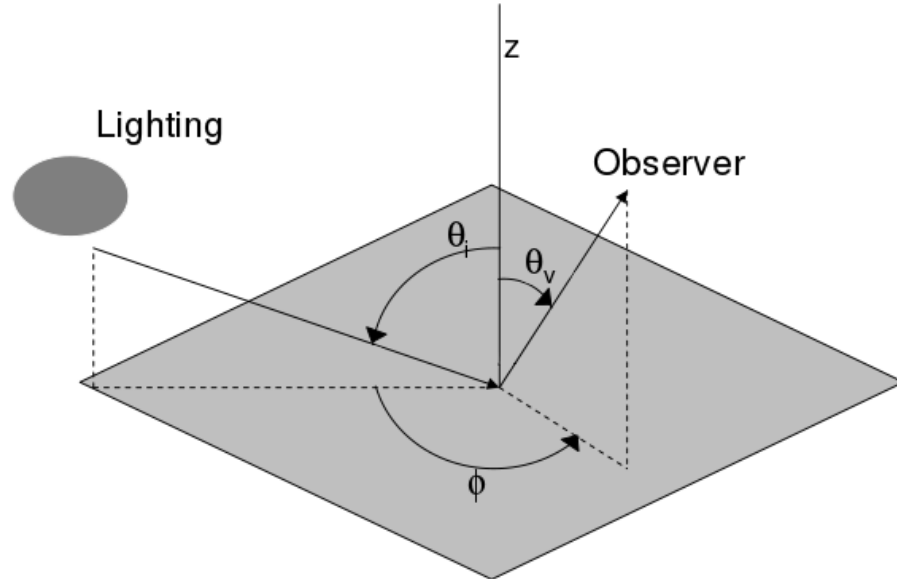


Figure 2.4: Presentation of the geometrical nomenclature in BRDF. Zenith angle θ and azimuth angle ϕ with index i for incident radiation angle and index v for the observers angle. Reprint from Dumont et al. [15]

2.4 Bidirectional Reflectance Distribution Function

For rough surfaces, the reflected radiation will be more diffuse and the Fresnel equations are not valid. A more sophisticated model is proposed, namely the bidirectional reflectance distribution function (BRDF), which describes the complete geometrical distribution of reflected radiance for any incident angle. How the reflected radiation is distributed can be interpreted as the "shininess" of a surface. In fig. 2.5 the diffuse, specular and a combination of these are presented. Nicodemus et al. [47] defined the BRDF as the ratio of the reflected radiance dL_v in direction (θ_v, ϕ_v) to the incident irradiance dE from direction (θ_i, ϕ_i) [68]:

$$f_v(\theta_i, \phi_i; \theta_v, \phi_v; \lambda) = \frac{dL_v(\theta_v, \phi_v)}{dE(\theta_i, \phi_i)} \quad (2.32)$$

Moreover, θ and ϕ are the zenith and azimuth angle, as seen in figure 2.4. A perfect diffuse surface, with homogeneous distribution of radiance regardless of how it is illuminated, is often referred to as a Lambertian surface [54].

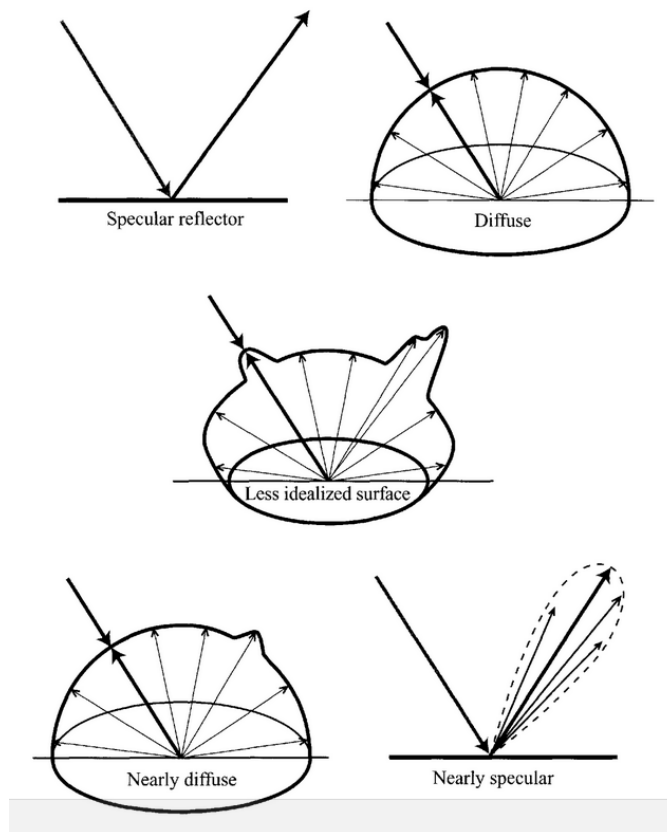


Figure 2.5: A surface can have various scattering characteristics from diffuse to specular. Reprint from Schott [66].

2.5 Green Functions

Green Functions is a mathematical tool to propagate the scattered wave from the surface to an arbitrary point in space. It utilizes the Huygens principle which states that every point on a planar wave surface at time t_0 can be considered as a source of a spherical wave. The wave surface observed at a later time $t > t_0$ will be the envelope of all the contributing sources at t_0 .

The extinction theorem explains the phenomenon that when light propagates from vacuum into non-vacuum material it slows down. This is because the sum of the incident light and the light waves generated by the affected dipoles in the non-vacuum material together creates a slower wave.

By equation (2.18) in the upper region, one can show that the fields satisfy the Huygens principle and extinction theorem [71, p. 17-18]. The Green function

of the reflected wave is expressed

$$\mathbf{E}^s(\mathbf{r}) = \int d\mathbf{s}' \{i\omega\mu\mathbf{G}(\mathbf{r}, \mathbf{r}') \cdot [\hat{\mathbf{n}} \times \mathbf{H}(\mathbf{r}')] + \nabla \times \mathbf{G}(\mathbf{r}, \mathbf{r}') \cdot [\hat{\mathbf{n}} \times \mathbf{E}(\mathbf{r}')]\}, \quad (2.33)$$

where

$$G(\mathbf{r}, \mathbf{r}') = \frac{1}{4\pi} \left(\mathbf{I} + \frac{\nabla \nabla}{k^2} \right) G'(\mathbf{r}, \mathbf{r}'). \quad (2.34)$$

\mathbf{I} is the unit dyadic and G' is the greens function for the Helmholtz equation

$$G'(\mathbf{r}, \mathbf{r}') = \frac{e^{ikG|\mathbf{r}-\mathbf{r}'|}}{|\mathbf{r}-\mathbf{r}'|}. \quad (2.35)$$

2.6 Random Rough Surface Scattering models

As scattering from a random rough surface is a rather complex process, it is challenging to create and compute rigorous models. One often make assumptions based on the surface characterizing parameters described in section 2.1 compared with incident radiation wavelength. Such models with a limited valid range are called asymptotic models.

For high-frequency radiation, the Kirchoff approximation (KA) model is common [51]. The KA is based on tangent plane approximation, where incident radiation is assumed to have short wavelength compared to surface topography. Thus, one can assume the reflection at every point on the surface to be specular, as if the point actually was a plane with slope equal to the slope at this point on the surface. A further simplification of the KA is called geometric optics (GO) or ray tracing, a model valid for wavelengths much shorter than surface characteristics. Some sources claims that it is valid if $\sigma_h > \lambda/4$ [51, p. 57], but the actual assumption is that the undulatory properties of the radiation can be neglected. In other words, the GO is valid only if the coherent contribution to the scattered field is very small compared to the incoherent.

2.7 Internal Scattering

Up to this point, the scattering of radiation encountering a rough or flat boundary between two homogeneous media has been described. Radiation transmitted through the surface of a porous media with continuous irregularities, may still be reflected back through the surface due to internal scattering. In general, Similar to how the Rayleigh roughness parameter described the scattering from a rough surface, we define the dimensionless quantity χ for

internal scattering. For spherical particles with radius r it is given by:

$$\chi = \frac{2\pi r}{\lambda} \quad (2.36)$$

In cases where $\chi \ll 1$, the wavelength is much smaller than the particles in the inhomogeneous media. For instance if light encounter a gas, Rayleigh scattering occurs. As the scattering efficiency is proportional to $1/\lambda^4$ [55] this explains for instance that short-wave blue light are more strongly scattered than the red light with longer wavelength, resulting in the sky appearing blue. In the intermediate case where $\chi \approx 1$ the term Mie scattering is used for describing the situation.

If $\chi \gg 1$ the wavelength of the propagating wave is much smaller than the particle radius and geometrical scattering occurs. This corresponds to the geometrical optics model for surface scattering, and is under the physical assumption of that the undulatory properties of the radiation can be neglected. Thus, the macroscopic case presented in section 2.3 will fully describe the process. To what extent radiation is scattered, absorbed or transmitted through the porous media will be determined of its geometrical properties and complex refractive indexes.

Because of its random nature, internal scattered radiation will be diffuse. Further, if a large fraction of the total scattered field comes from internal scattering, the total field is expected to be diffuse [68].

/3

Altimetry

Altimetry is the science of determining elevation. A wide range of measurement principles can be applied for deciding the altitude of an aerial vehicle. The requirements of instrumentation when it comes to accuracy, weight, volume, computational cost, range, ability in dark and non-transparent environments and production cost are decisive factors.

3.1 GPS and Barometer Based Altimetry

Barometric altimeters and Global Positioning Systems (GPS) are often considered as default instrumentation on UAV platforms to provide estimation of altitude. The GPS requires communication with satellites, which makes it vulnerable for signal drop out. Barometric altimeters have errors on decimeter scale [75], but is also sensitive to turbulence and drift in pressure, such that it needs calibration. During low altitude hovering and takeoff/landing, the accuracy demands are in general on centimeter level. One can enhance the performance of barometer/GPS altimetry by sensor fusion (eg. Kalman Filtering) with an internal measurement unit (IMU) that consists of motion (accelerometer) and rotational (gyroscope) sensors. Including a time-of-flight (TOF) pulsed radar altimeter will increase accuracy even further [12].

3.2 Rangefinders

3.2.1 Time of Flight

The principle of time-of-flight (TOF), or pulsed rangefinders, can be applied for both acoustic and EM waves, most common in microwave and infrared bands of the spectrum. The system outputs a short pulse and a receiver detects an echo. The time between these events Δt will define the distance d :

$$d = \frac{c\Delta t}{2}. \quad (3.1)$$

c is the speed of the propagating wave, and the factor 2 refers to the round trip.

Emitting short pulses implies large amount of energy to provide sufficient signal power compared to background noise, but at low average power consumption. The latter is preferable for UAV instrumentation and to ensure eye safety.

The rise- and fall-time of a square pulse and the width of a gaussian pulse will determine the longitudinal accuracy of the system. These quantities are proportional to the bandwidth of the signal, analogue with fundamental signal processing theory which states that a sharp impulse in time-domain has a wide frequency content. A simple approximation of the direct relation between bandwidth BW and range resolution δ_r is given by [13]:

$$\delta_r \approx 2BW \cdot c \quad (3.2)$$

Thus, high bandwidth ensures high range resolution. Electronics for amplification and sampling of a broadband signal are expensive, and is a significant drawback of the TOF principle.

3.2.2 Frequency Modulated Continuous Wave

To avert the practical issues that come along with handling a broadband signal, the frequency modulated continuous wave (FMCW) technique can be utilized by rangefinders. The signal transmitted is constant in amplitude, but the frequency is swept from f_1 to f_2 over the time t_s . The reflected signal is mixed with the transmitted, and they form a beat frequency f_d [10]:

$$f_d = \frac{\Delta t(f_2 - f_1)}{t_s} \quad (3.3)$$

f_d can be measured by a spectrum analyzer and Δt is the time of flight, and the distance to the target can be calculated by equation (3.1).

3.2.3 Optical Triangulation

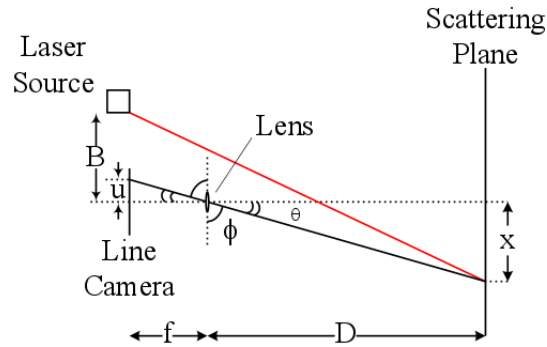


Figure 3.1: Concept of optical triangulation [4, p. 5]

Optical triangulation estimates distance by emitting a narrow-banded continuous waveform from a laser source. The backscattered radiation is then focused by a lens into a 1D line camera, the location u of the most illuminated pixel can then resolve the distance D by:

$$xf = uD \quad (3.4)$$

where f is focal length, u is illuminated pixel and x is horizontal distance from the lens to reflection point on the ground, as seen in figure 3.1. From equation (3.4) it is clear that for large altitudes D , u will be small, and thus high resolution of the line array camera is required to maintain accuracy. This implies that this approach is suited only for small variations at low altitudes. Optical triangulation rangefinders can be more accurate than those based on TOF, as a narrow banded signal is easier to preserve than a broadband pulse.

3.2.4 Ultrasonic Rangefinders

Ultrasonic rangefinders are based on the TOF principle. They emit short pulses of acoustic waves towards a target, and measure the time of arrival of the echo pulse. Reflectance of a wave propagating in a medium with acoustic impedance Z_1 onto a medium with acoustic impedance Z_2 separated by a surface is given by:

$$R = \frac{Z_1 - Z_2}{Z_1 + Z_2} \quad (3.5)$$

The acoustic impedance can be interpreted as how a given medium opposes to an incident pressure field. Compared to TOF rangefinders based on EM

waves, sampling, amplification and other electronics are manageable due to the relatively slow propagation speed of sound compared to light. As the signal is acoustic, turbulence from rotors, as well as wind and vibrations are factors of concern.

3.3 Systems for Target Localization

There are a range of systems to provide real-time data on the position of a vehicle relative to its surroundings. Some systems aim to create a full 3D map of the local environment, and thereby vehicle localization. Others have less sophisticated approaches for the purpose of obtaining estimations of altitude and attitude¹ of the vehicle.

3.3.1 Simultaneous Localization and Mapping

The technique of simultaneous localization and mapping (SLAM) is widely used in both ground-based and aerial platforms to construct a mapping of an unknown environment and the localization of the vehicle [27]. Several different sensor systems are used for data acquisition. With one or several passive cameras, one can by computer vision techniques detect features on the ground to create a 3D model of the surroundings. This technique is computationally costly and memory demanding, as a stream of high-resolution images must be processed by algorithms on the fly. The required visual contact between the target and the passive cameras implies that the system fails in dark or non-transparent conditions. Computer vision algorithms require some kind of features in the image for obtaining reference points. Such features can be points, edges, regions or anything that can be separated from its neighborhood. Snow cover, desert and other homogeneous surfaces have few landmarks and will, therefore, be challenging for computer vision algorithms.

Active sensors like lidars, sonars and similar instruments can also be used for the purpose. Some of the above use the TOF principle to measure the range to the target, and by sweeping over an area, will provide a map. Moving parts are power consuming and considered as a drawback for a standalone platform like a UAV.

To enhance the performance of the camera approach, it has been developed a hybrid system where a circle illuminates the ground and appears as an

1. The orientation of an aerial vehicle is called attitude, often divided into pitch, yaw and roll in the 3D case.

artificial landmark [45]. The circle is detected by a camera, and by analyzing the size and shape of the circle, altitude and attitude can be determined.

3.3.2 Array of TOF Sensors

In this thesis we intend to develop a new system that aims to be simpler than comprehensive SLAM techniques, and still retain the robustness of an active sensor system. This system consists of an array of TOF sensors. If the surface is assumed to be locally flat, information about both altitude and attitude can be provided with only two sensors in the 2D case, and three in the 3D. In the following derivation, it is the relative attitude between the ground and the UAV that is of interest. When directing the radar beam onto the surface, the absolute angle is irrelevant. The altitude h is here defined as the distance measured perpendicularly from the UAV to the ground as if the UWiBaSS microwave (MW) radar is fixed under the UAV. h will be an estimation of where the surface is on the radar image. If the UWiBaSS radar is mounted on a pivoted platform, it is actually the relative angle between this platform and the surface that is of interest, and not the UAV tilt angle. However, in this section we assume that the radar is fixed under the UAV.

We will present two configurations of the 2D problem. Case 1: one altimeter is directed perpendicular to the UAV and one forward. Case 2: one altimeter forward and one backward. Figure 3.2 shows the two setups and table 3.1 describe the nomenclature. It is important to note that the thin black line in figure 3.2 does not necessarily represent the horizontal axis, but is aligned with the UAV. Thus, when $\phi = 0$ the local surface tilt is equal to the tilt of the UAV, but they may both have a tilt relative to the horizontal axis.

Table 3.1: Nomenclature of the array of two rangefinders. (D+F) is downward + backward configuration of altimeters and (B+F) denotes backward + forward.

Symbol	Description
θ	Angle between beams
ϕ	Relative angle between the surface and the UAV
α, β	Angles used for calculations.
s	Distance between the illuminated spots on surface
d_1, d_2	Measured distance by the forward and backward altimeter (B+F)
d_f	Measured distance by the forward altimeter (D+F)
h	Height. Distance measured to the ground perpendicular to the UAV

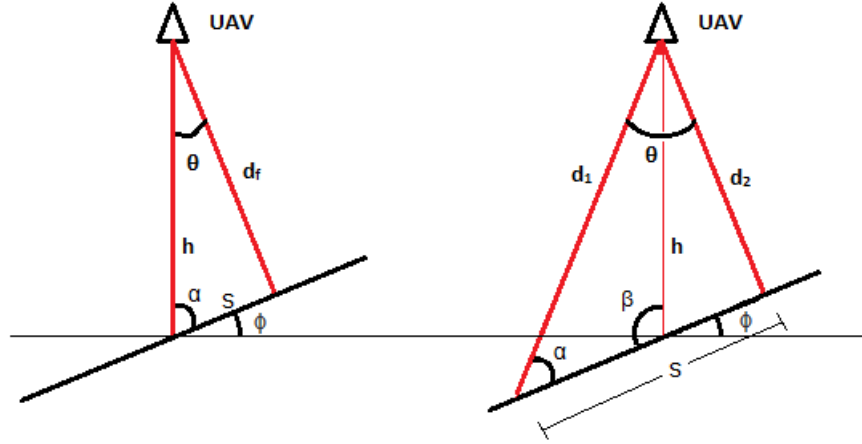


Figure 3.2: Principle sketch of the 2D problem for an array of two TOF sensors. It is solved by two configurations; (left) downward + forward facing altimeters or (right) backward + forward. Thick red lines are altimeter beams, thick black line denotes the surface and thin black line is the axis aligned with the UAV. ϕ denotes the angle between surface and the UAV.

Downward and Forward Pointing Direction

With the downward + forward altimeter configuration the height h is directly measured by the downward facing altimeter. To obtain estimation of the tilt angle ϕ we need to include the the distance d_f estimated by the forward facing altimeter. By the law of cosines:

$$s = \sqrt{h^2 + d_f^2 - 2hd_f \cos\theta}, \quad (3.6)$$

and by the law of sines:

$$\alpha = \arcsin\left(\frac{h \sin\theta}{s}\right). \quad (3.7)$$

The relative angle in radians is given as:

$$\phi = \frac{\pi}{2} - \alpha. \quad (3.8)$$

Note that ϕ has positive direction counter-clockwise and is zero when the surface is perfectly aligned with the UAV.

Backward and Forward Pointing Direction

In the backward + forward setup height h is not measured directly, thus we need to derive an algorithm to obtain h as well as ϕ based on the measured

values of d_1 and d_2 . We start similarly by finding s by the law of cosines:

$$s = \sqrt{d_1^2 + d_2^2 - 2d_1d_2\cos\theta}, \quad (3.9)$$

and by the law of sines:

$$\alpha = \arcsin\left(\frac{d_2\sin\theta}{s}\right). \quad (3.10)$$

Also by the law of sines, the altitude h of the vehicle is given:

$$h = \frac{d_1\sin\alpha}{\sin\beta}, \quad (3.11)$$

and the relative tilt angle can be found by:

$$\phi = \beta - \frac{\pi}{2}. \quad (3.12)$$

To be able to estimate h and ϕ both altimeters must be operating. Note that for case 2, the angle $\alpha = \phi + \theta$. Hence, to avoid a decreasing backscattered signal due to low-grazing angles θ should not be too large, and diffuse scattering characteristics will ensure acceptable strength of signal. Also, if the beam pattern of the altimeter is divergent, this can affect the accuracy at low-grazing incident angles, since the illuminated spot will be covering a large area. An altimeter with pencil beam radiation pattern, that tolerates low-grazing incident angles, therefore is required.

/4

Classification of Seasonal Snow and its Optical Properties

The physics of snow is complex and under constant change in time and space with a number of variables. Discriminating between snow classes is not obvious and for characterization some simplifications must be made. The most prominent features required to be assessed for this purpose are grain size and shape, temperature, liquid water content and density. In addition, parameters like terrain and layering of the snow cover will define the risk the of an avalanche to occur. This section will first cover the basic physics of snow, followed by a discussion of its optical properties. At last, a brief introduction on avalanches is given, as this was an important motivation behind the thesis.

"The International Classification for Seasonal Snow on the Ground" [18] sums up a consensus in how to classify seasonal snow. They operate with the main categories listed in table 4.1 and grain size is classified as listed in table 4.2. When and where to expect the different types to appear is best understood by looking into the changes of snow crystals due to ambient weather conditions. This process is called metamorphism [38].

Table 4.1: Classification of seasonal snow [18]

Class	Code
Precipitation Particles	PP
Machine Made Snow	MM
Decomposing and Fragmented precipitation particles	DF
Rounded Grains	RG
Faceted Crystals	FC
Depth Hoar	DH
Surface Hoar	SH
Melt Forms	MF
Ice Formations	IF

Table 4.2: Classification of grain size [18]

Term	Size[mm]
very fine	< 0.2
fine	0.2 - 0.5
medium	0.5 – 1.0
coarse	1.0 – 2.0
very coarse	2.0 – 5.0
extreme	> 5.0

4.1 Metamorphism of Snow

Snow crystals arise first in clouds, where supersaturated conditions permit precipitation particles with complex geometrical shapes to be created, such as stellar dendrites [18]. When accumulated on the ground, these particles can be fragmented into smaller particles, but still with a large surface-to-volume ratio. From this point on, the crystals will immediately start to change due to heat flow and excessive pressure. The metamorphism of snow can be divided into three main types, namely dry, wet and temperature gradient [38].

4.1.1 Dry Metamorphism

The precipitation particles, with very high surface to volume ratio, will not maintain its shape for long during normal conditions. As implied by figure 4.1, grains, or part of grains, which have the smallest radius will melt first. Thus, geometrically complex grains are transformed into rounded grains as time goes on. The process will be slow, if the ambient temperature is low [38].

4.1.2 Wet Metamorphism

When the temperature rises above the freezing point, snow gets wet. Wet snow consists of ice, air and liquid water. Similar to the dry metamorphism, small grains will melt first and the average grain size will grow [38], but now the temperature is higher and the process will be much more rapid. As the metamorphism goes on for a long time under relative high temperatures, the snow will appear as incohesive "slush". This is because the bonds between the grains melt [38].

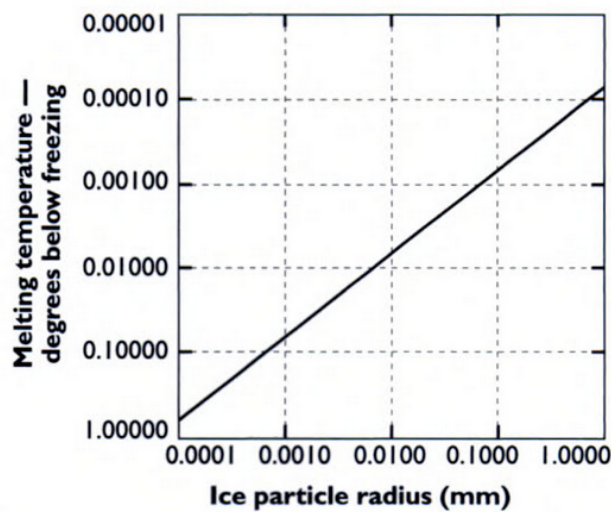


Figure 4.1: The relation between melting temperature versus grain size. Reprint from McClung and Schaerers [38].

4.1.3 Temperature Gradient Metamorphism

During cold, clear winter nights, air temperature often drops well below zero centigrades. The ground under the snow cover is well insulated and will have a more stable temperature. Thus, when the temperature difference from ground to air is sufficiently high, water vapor will start to flow. The water vapor will eventually condensate on crystals inside the snow pack, and create faceted crystals, and eventually depth hoar [70]. When the crystals grow in size, they will give instabilities in the snow pack. This is because the sintering process goes to the inverse 4th power of the grain size [70], such that layers of large grains will create persistent weak layers. Sintering is the process where ice-bonds form between grains and increases the mechanical strength of the snow.

In general, temperature gradient metamorphisms occurs at temperature gra-

dients larger than $10\text{ }^{\circ}\text{C}/\text{m}$ [70]. Thus, where the snow cover is shallow, it is more likely to appear.

Formation of Surface Hoar

A related phenomenon to temperature gradient metamorphism is the formation of surface hoar. Surface hoar can appear if the air is sufficiently humid ($>70\%$) and the temperature gradient is relative high [70]. Then, the water vapor will sublimate on the cold surface of the snow crystals. The surface hoar crystals can grow up to centimeter-level, as seen in fig. 4.2. Buried layers of surface hoar can give persistent weak layers and instabilities in the snow pack, as its size indicates long sintering time [70].



Figure 4.2: (left) Photo of surface hoar February 9th in Tromsø, after a cold, humid period. (right) Shows that the cup-formed crystals, typical for both surface and depth hoar, have grown to about one centimeter.

4.2 Optical Properties

Snow and ice are covering the surface of the earth's polar areas, and in the winter season also the surrounding areas. Snow and ice have a very high albedo¹, and have potential to strongly affect the global energy budget. It has for that reason been of interest for scientists to describe their reflective properties in the solar spectrum (ultraviolet (UV) to infrared (IR)). Clean snow appears white for the human eye, which implies that the reflection coefficient is high throughout the visible spectrum. This can be explained by that ice is very transparent at these frequencies, and the probability of a photon to be

1. Albedo is by Earth and Space Research Institute defined as "the fraction of solar energy reflected from the Earth back into space" [16].

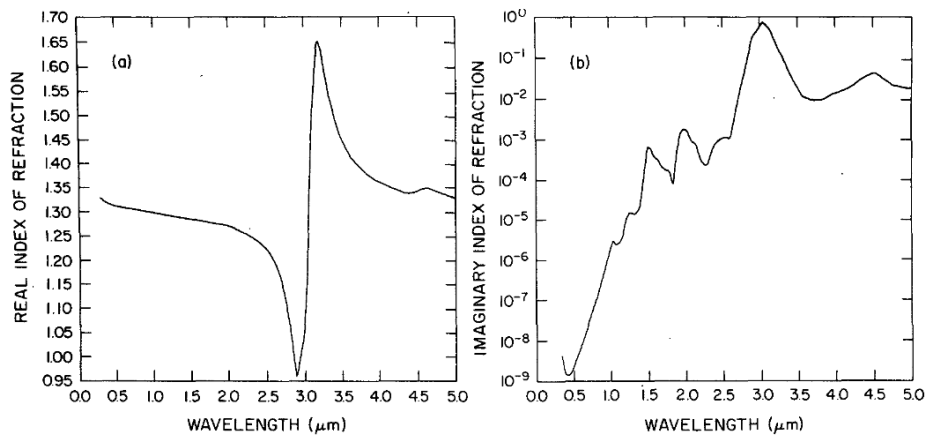


Figure 4.3: Real and imaginary refractive index of ice at -7°C in the optical spectrum. Reprint from Warren et. al [73]

absorbed, even for large grains, is very small. However, as we see from figure 4.3(right) the imaginary part of the refractive index increases for ice in the near-infrared (NIR), and thus is more absorbing. Further, 4.3(left) show that the real part of the refractive index is relative constant over the NIR band. This implies that when grain size increases, the probability of a photon to be absorbed will also increase, as there are fewer air-ice interfaces for be reflected from, and more ice to be absorbed in [31]. Implications of this phenomena are showed in figure 4.4 where the reflectivity of snow grains of various sizes are plotted from the visible spectrum into the infrared region. It shows that up to ~ 800 nm the reflection is independent of grain size, but then reflection turns to be sensitive to grain size. The effect is greatest in the NIR part of the spectrum.

4.2.1 Optical Equivalent Grain Size

We have seen that the optical reflection characteristics of the snow is first and foremost determined by grain size. However, as explained earlier in this chapter, snow grains can appear in various forms from 2D stellar dendrites to clusters of spheres. Therefore, it is convenient to define an "optical equivalent grain size" which provides a generic way to define the size of an arbitrary formed grain. Scattering models estimates snow grains with equivalent spheres because this simplifies the scattering problem. Mugnai and Wiscombe [42] showed that spheroids can be modeled as equivalent spheres if they are randomly oriented. Further, Greenfell and Warren [20] found that by replacing a non-spherical grain with a cloud of spheres with the exact same surface-to-volume ratio the scattering properties where preserved. This approach gave better results than

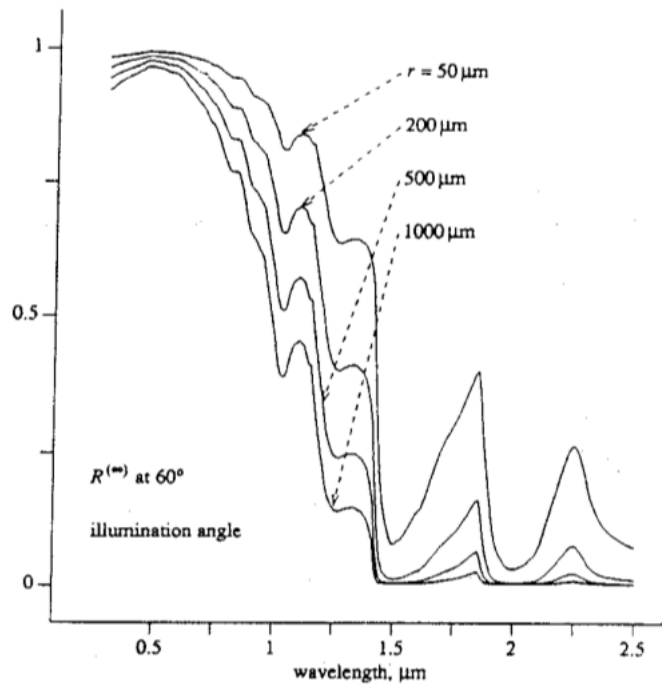


Figure 4.4: Reflection coefficient on the vertical axis plotted versus wavelength for different grain sizes. This a reprint from Nolin [48].

replacing the non-spherical grain with a sphere with equal volume, or a sphere with equal surface area, as they would correspondingly alter the surface or volume of the non-spherical grain. To obtain this, the number of equivalent spheres could be different than the number of non-spherical grains, as showed in figure 4.5. Here, 10 hexagonal columns model 23 spheres to preserve the surface-to-volume-ratio.

The implications from fig. 4.4 is utilized by researchers to perform so-called grain size mapping, where spaceborne active sensors in the frequency spectrum especially sensitive to grain size are used, eg. by Nolin [48] who uses 1064 nm. The reflection measured will, therefore, depend on the grain size at the illuminated spot on the surface, and if sufficiently calibrated, one can estimate the grain size [48]. However, it is important to note that grains with very large surface to volume ratio, ie. precipitation particles and surface hoar, will have a small optical grain size compared how large they appear on a grain classification board (see fig. 4.2 (b)).

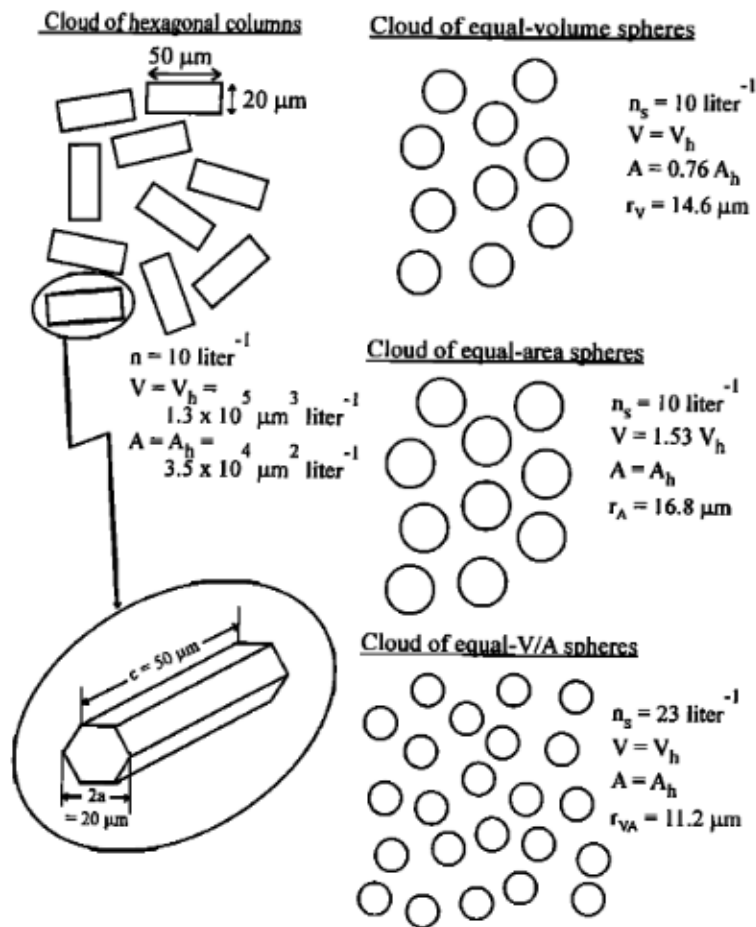


Figure 4.5: In order to model non-spherical grains as spheres to simplify scattering models, it was proposed to replace non-spherical grains with a family of spheres with equal surface to volume ratio. The figures show how hexagonal columns can be replaced with spheres with equivalent volume (top), equivalent surface area (middle) and equivalent surface to volume ratio (bottom). Reprint from Greenfell and Warren [20].

4.2.2 Geometrical Surface Characterization

As came clear in section 2.1, the feasible way give a geometrical description of a rough surface is by its statistics. Moreover, a snow surface can have roughness on several scales, like a sea wave that has large swell with smaller ripples. The grain size and shape, affected by metamorphism, will define the micro-scale structure of the surface. Larger structures can typically be caused of wind deposited snow. Rees [54], who presents both his and others work, states that a typical spatial extent of the RMS measurements are "few tens of centimeter to a meter or so". Typical RMS height (see eq. (2.2)) of a snow surface is found

to range from 0.5-30 mm [59, 60, 54].

The autocorrelation function (ACF) with its related correlation length l_c , as defined in section 2.1.1, describes how correlated the surface height is to itself due to a horizontal shift. Typical values for l_c is 30 -300 mm [59, 60, 54]. The correlation length is strictly related to grain size [69, 35, 28]

4.2.3 Bidirectional Reflectance Distribution Function

Only by looking at a snow surface, one can tell that it under normal conditions is a diffuse scatterer for visible wavelengths. In order to simplify their models, researchers often view the scattering as strictly Lambertian, even though this is not the case according to Li et. al [33]. Hence, to fully describe the geometrical radiation pattern, a BRDF should be obtained, either experimentally or by simulations.

Figure 4.6, a result of work done by Kokaniovsky et al. [30], shows a simplified version of the BRDF where a snow surface is illuminated by the sun at $\theta_i = 54^\circ$ zenith angle. The reflection is measured at various zenith angles at 180° azimuth angle. The numerical models are based on an asymptotic radiative transfer model. The illuminated snow surface consisted of rounded and faceted grains covered with a 2 mm layer of precipitation particles. The experimental measurements indicate the surface to be a diffuse scatterer.

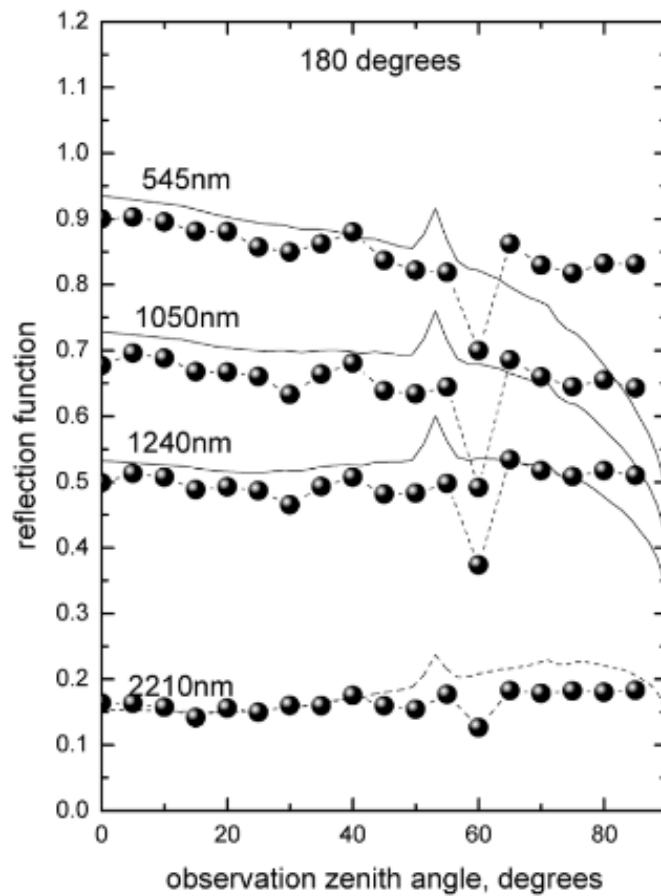


Figure 4.6: Reflection measurements (dots) compared with numerical models (lines) for various wavelengths in the visible and NIR spectrum of a snow surface. It is illuminated by sun in zenith angle 54° observed from zenith angle $0-90^\circ$ and azimuth angle 180° . Reprinted from Kokaniovsky [30].

4.2.4 Optical Attenuation in Free Space

An increase in the probability of an avalanche to occur is often connected to heavy snow or rain (dry and wet slab avalanches) [38]. Thus, it is preferable that the Ultra Wide-Band Snow Sensor system is able to perform under such conditions.

An important property of optical waves propagating in free space² is that they are attenuated by air particles like dust, smog, fog and hydrometeors (falling

2. Free space could be air, vacuum or similar

rain or snow). This corresponds to the reduced visibility a human eye will experience under the mentioned conditions. Optical remote sensing applications differ from RF (Radio Frequency) sensors as they can not penetrate clouds [74]. In the case of a low altitude (<10 m) hovering UAV, it is hydrometeors and fog that are most challenging. This field is also studied as a limiting factor of free space optics (FSO). FSO is presented as a low cost, broadband transmission link where an optical receiver is placed in line of sight of a transceiver and the wave propagates in free space, contrary to a fiber cable. Nebolini and Capsoli [46] conducted an experiment with measuring the attenuation of a 785 nm FSO transmission link, they found that: "a laser beam traveling through falling snow experiences attenuation levels often exceeding -45 dB/km" [46]. There are also developed empirical models for attenuation of optical waves in free space. Carbonneau's model for rain attenuation states [44]:

$$att_{rain} = -1.076 \cdot R^{0.67} \quad [\text{dB/km}] \quad (4.1)$$

where R is rainfall rate [mm/hour]. For snow the attenuation rate is given [44]:

$$att_{snow} = -aS^b \quad [\text{dB/km}] \quad (4.2)$$

S is snowfall rate in [mm/hour]. Parameters a and b for wet snow are

$$a = 0.0001023 \cdot \lambda_{nm} + 3.78555 \quad (4.3)$$

and dry snow

$$a = 0.0000542 \cdot \lambda_{nm} + 5.49588 \quad (4.4)$$

The models are not rigorous as the parameters assume spherical grains. However, it will give some indication on what degree of attenuation to expect.

Case Study: Attenuation of 905 nm

We did some simple calculations to evaluate how much attenuation we can expect for 905 nm radiation at various precipitations rates. "Heavy Rain" has no rigid definition, but it is for instance defined as precipitation rate of > 7 mm/hour by official Canadian sources [49]. Attenuation rates from eq. (4.1) and (4.2) calculated at various precipitation rates are presented in figure 4.7. It is clear that dry snow causes most attenuation, this was expected as heavy snow affects the human visibility more than heavy rain. At ten meters with precipitation rate 4 mm/hr, the attenuation is

$$att_{10} = \frac{-40\text{db/km}}{100\text{m}} = -0.4\text{dB}, \quad (4.5)$$

which correspond to percentage power loss of 1%. Thus, free space attenuation will have a small influence on the reflected signal, when considering relatively low altitudes for UAV hovering.

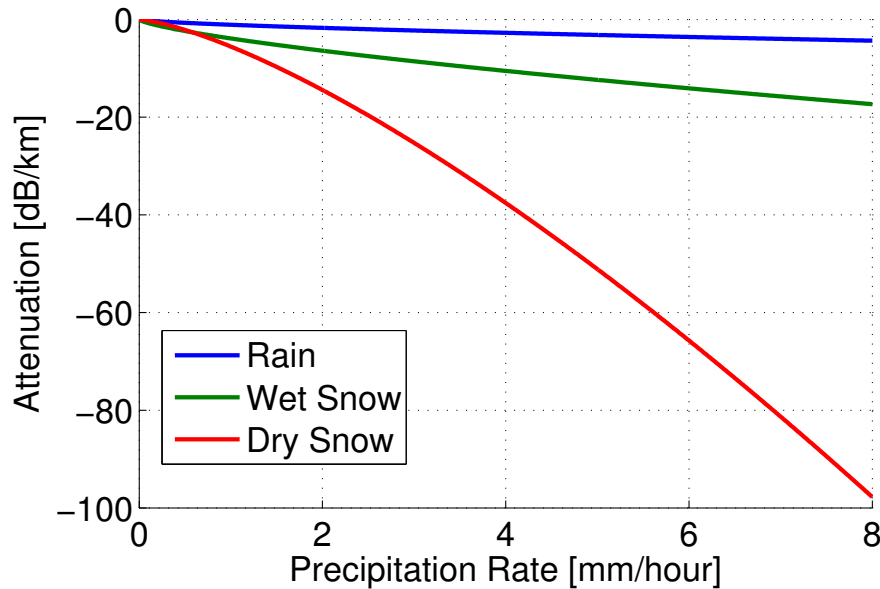


Figure 4.7: The optical attenuation of 905 nm wave propagation in free space due to precipitation at various rates.

4.3 Avalanches

There are two main types of avalanches, slab and loose. Slab avalanches occur when cohesive plates of snow slide down the mountain as a unit. This is the by far most dangerous type and the one usually considered when talking about avalanche risk. Loose avalanches are caused by uncohesive, dry or wet snow sliding. They start from a point and fan out as they descend [70]. The latter is considered as less harmful, as they are traveling in lower speed and, hence are easier to avoid. For that reason, slab avalanches are the focus in this thesis.

To cause a slab avalanche the following is required [70]

- A slab - A cohesive, relatively hard layer (often 1F-4F, see section 8.2)
- A weak interface

- A harder bed for the slab to slide on.

In addition to the snow condition requirements, a slope of $> 30^\circ$ and some kind of external trigger, like a skier or a snowmobile, must be present for a slab avalanche to occur. A sufficient cohesive slab is often generated by wind deposited snow. When the wind has deposited snow, it is usually not well connected to its underlying bed for a couple of days. If the bed is covered by larger grains, as surface hoar, faceted crystals or even light density precipitation particles, this process of sintering will last much longer and, therefore, cause persistent weak layers [70]

/5

Choice of Altimetric System

In this chapter we will sum up the most prominent requirements of the altimetric system. To choose the right altimeter related to application, we have looked closer into several typical off-the-shelf altimeters, presented briefly in table 5.1. Obviously, they are only a small part of the commercial market, but they are representative for pros and cons with the different technological concepts presented in chapter 3. The accuracy and reliability requirements rule out GPS and barometric systems, and they will not be given any further attention. Throughout this the chapter, features of the altimeters will be considered in regards to the operational requirements of the altimetric system. At last, the most promising altimeter will be chosen.

Table 5.1: List of some typical, off-the-shelf, high accuracy altimeters and rangefinders available for mount on an UAV platform.

Altimeter Type	Model/Manufacturer	Wavelength
Radar Altimeter	Miniature RA/Roke [58]	0.39 cm
Infrared TOF	SF10/Lightware [34]	900 nm
Opt. Triangulation	Microtrak 3/MTI [41]	670 nm
Lidar	RPLIDAR/RoboPeak [56]	785 nm
Acoustic TOF	LV-MaxSonar/Matibox [36]	0.81 cm

5.1 Decisive Factors

In order to achieve the goal of a robust altimetric system with accuracy on centimeter level over a snow covered surface, we stated the following factors as decisive.

5.1.1 Accuracy and Range

Accuracy of the altimeter should at least overcome the UWIBaSS sensors range resolution of 5.3 cm [62], but preferably be within ± 2 cm. In table 5.2 we see that optical triangulation, can be accurate on millimeter level. This is assumed excessive for the purpose, as snow often has height RMS value $\sigma = 0.5 - 30$ mm. Thus, accuracy around 1 cm is sufficient. Feasible range of a future version UWIBaSS sensor is stated to be up to 10 m [62]. Thus, the altimeter should perform beyond this range.

Table 5.2: Comparison of the considered altimeters in regards to accuracy and range given in manual.

Altimeter Type	Accuracy	Range
Radar Altimeter	2 cm	0.02-100 m
Infrared TOF	1 cm	0-25 m
Opt. Triangulation	3.8 μm	0-0.25 m
Lidar	1 cm	0.2 - 6 m
Acoustic TOF	2.5 cm	0-6.45 m

5.1.2 Scattering and Reflectivity

Scattering and reflectivity are factors that will affect how robust a rangefinder altimeter is due to variations in attitude and altitude of the UAV. The scattering characteristics can be diffuse, specular or a combination of the two. A specular reflection will be optimal as long as the altimeter is pointed orthogonally towards the ground, as most of the energy will be reflected back in the direction of the receiver. On the other hand, a very rough surface will increase the probability of receiving a detectable signal, even if the altimeter is not oriented towards the ground. For the specific application of a low altitude UAV altimeter, diffuse scattering is preferred, as this will make it more robust due to attitude fluctuations, even though the overall range of the altimeter might be reduced.

As we saw in chapter 4, the scattered energy may originate from surface scattering or internal scattering. If internal scattering is reflected back, it is in general

diffuse. Whether the surface scattering is diffuse is decided by the wavelength of emitted radiation relative to the roughness of the reflecting surface. One way to define this, is by the Rayleigh roughness presented in section 2.1.2. We know from equation (2.9) that when $R_a > \pi/4$ a surface is defined as very rough. From table 5.3 it is clear that the altimeters emitting optical or near-infrared radiation overcome this requirement by far, and will make sure that scattering is diffuse, even when the snow surface is at its smoothest at $\sigma_h = 0.05$ cm. It is important to emphasize that contrary to microwaves, most of the reflected optical radiation will originate from internal scattering [54], also implying diffuse scattering. The acoustic and radar altimeters however, have $R_a < \pi/4$ when encountering a smooth snow surface, and are thus not defined as rough by the Rayleigh criterion.

Table 5.3: Comparison of the altimeters due to its scattering characteristics. The Rayleigh Roughness (RR) parameter is calculated for a typical and a very smooth snow surface. The limit to qualify as rough is $R_a > \pi/4 \approx 0.79$

Altimeter Type	R_a typical ($\sigma_h = 0.5$ cm)	R_a smooth ($\sigma_h = 0.05$ cm)
Radar Altimeter	0.8055	0.08055
Infrared TOF	$3.4905 \cdot 10^4$	$3.4906 \cdot 10^3$
Opt. Triangulation	$4.6889 \cdot 10^4$	$4.6889 \cdot 10^3$
Lidar	$4.0020 \cdot 10^4$	$4.0020 \cdot 10^3$
Acoustic TOF	3.8785	0.38785

According to section 4.2 radiation in the visible and into the NIR part of the spectrum has a near-one reflection coefficient. From around 1000 nm the reflection coefficient is lower. As discussed in section 2.3, microwave radiation has lower reflection coefficient, particularly light dense powder snow is nearly invisible by radar.

5.1.3 Beam Divergence

An array of rangefinder altimeters would be able to give estimations of the UAVs attitude in real time as presented in section 3.3.2. In this application it is strongly preferable with a narrow beam. If the illuminated area on the ground is large, it will increase the probability of error in range estimation. In general, optical lenses are very effective, making the radiation close to pencil beam. As table 5.4 implies, lenses are not as effective in the microwave band, hence the optical altimeters have the preferable beam divergence.

Table 5.4: Comparison of beam divergences of the given altimeters.

Altimeter Type	Beam Div.
Radar Altimeter	20-40 ^o
Infrared TOF	0.3 ^o
Opt. Triangulation	0.012 ^o
Lidar	1 ^o
Acoustic TOF	<30 ^o [22]

5.1.4 Physical Size and Power Consumption

When adding a payload to an UAV platform, it is of great importance to avoid bulky and very power consuming alternatives. In table 5.5 some relevant features are presented for the same altimeters that are considered earlier in the chapter.

Table 5.5: Comparison of altimeters size, weight and power consumption given in the manual.

Altimeter Type	Size [mm]	Weight [g]	Avg. Power Consumption
Radar Altimeter	140 × 75 × 46	400	3 W
Infrared TOF	30 × 57 × 50	35	0.6 mW
Opt. Triangulation	107 × 110 × 38	-	2.8 W
Lidar	-	170	1.15 W
Acoustic TOF	22 × 20 × 15	4.3	1 mW

5.2 Discussion

Some main conclusions can be drawn from chapter 5.1:

- Optical Triangulation provides very high accuracy, but only within small range. The other altimeters considered have sufficient accuracy and range.
- Altimeters radiating in the optical spectrum will ensure diffuse scattering, and hence be robust to attitude fluctuations of the UAV, compared to the radar and acoustic altimeter.
- The altimeters in the optical spectrum have close to pencil beam, ideal for use in an array setup. Radar altimeter have a significantly more diverging beam.

- None of the considered alternatives are very bulky or power consuming, but the NIR TOF and acoustic TOF are especially well suited for mount on UAV.

Thus, the SF10 NIR TOF rangefinder from Lightware Optoelectronics is chosen as it is neat, accurate and with scattering characteristics considered well suited for the purpose. However, most important is the promising high reflection coefficient of 905 nm radiation when encountering a snow surface. In the rest of this thesis, the SF10 altimeter will be presented in detail, verified experimentally and discussed.

Part II

System Description and Implementation

/6

SF10 Lightware Rangefinder

The SF10 is an altimeter based on TOF principle in the NIR spectrum delivered by Lightware Optoelectronics¹. It is a compact, accurate instrument well suited for mount on an UAV. To interface with the UAV control system it is compatible with the I2C communication protocol, serial and analog. It can also be interfaced through Lightware Terminal (LT) software that provides range, signal strength and an image of the transmitted and received pulses. More specifications about SF10 can be found in table 6.1.



Figure 6.1: The SF10 rangefinder [34]

1. www.lightware.co.za/

Table 6.1: Specifications for the Lightware SF10 [34]

SF10 sensor parameter	Value/feature
Laser wavelength	905 nm
Range	<25 m
Resolution	1 cm
Update rate	32 Hz
Accuracy	±5 cm
Weight	69 g
Interfaces	I2C, Serial, Analog
Laser power	10 W peak, <0.6 mW average
Pulse width	<20 ns
Pulse frequency	<36 kHz
Beam divergence	0.4°
Operating temp	0-40°C

6.1 Signal Sampling

In a TOF rangefinder system, the information is carried by a pulse. The accuracy of the system is related to the rise- and/or fall-time of this pulse.

The most accurate and intuitive way to sample the signal is by real time sampling, where a single shot pulse is emitted and the signal is sampled in real time. The method requires electronic circuitry to amplify and sample the broad banded signal. The required sampling rate is given by Nyquist sampling theorem[37], which states that to reconstruct a signal:

$$f_s > 2f_{max}, \quad (6.1)$$

where f_s is the sampling frequency, and f_{max} is the maximum frequency of the signal. To handle single shot signals is very costly. To overcome this, one can trigger multiple pulses and sample one new data point for every new pulse (see figure 6.2). Together these data points will assemble to a complete waveform. The method is called sequential time equivalent sampling (SETS) and is a less costly way to do high frequency sampling, but at the cost of slower pulse update rates [65].

Prominent features of the SETS are that the target is assumed stationary over the period of acquisition of a single waveform, to be able to give a proper reconstruction of the true signal. At the receiver, pre-sampling amplifiers are often avoided to maintain bandwidth. This will decrease the signal-to-noise ratio (SNR), from the principle that in a cascaded system, the signal amplification should appear near the front-end to avoid noise to accumulate when the

signal is weak [52, p. 505]. SETS will in general yield higher time resolution, compared to single shot sampling [65]. The pulse frequency given in table 6.1 will not represent the frequency of new distance reads to appear. We measured the rate of distance read to be 32 read/sec, around a thousand times slower than the pulse frequency. Thus, SETS will slow down this rate significantly compared to single shot sampling.

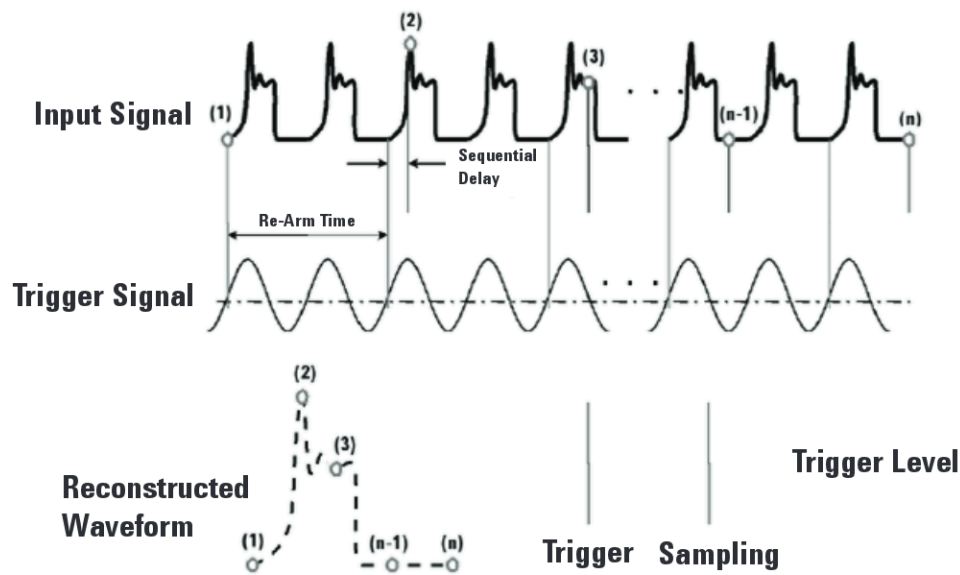


Figure 6.2: Principle of sequential equivalent time sampling. Reprint from Agilent Technologies [3].

6.2 Noise

In electronic components, one often assumes a linear and deterministic relationship between the input and output, where the input can be determined by the output. However, all systems have a power range of operation that is limited by the noise floor at the lower end and maximum power output at the upper end, as seen in figure 6.3.

The dynamic range of the SF10 must not be confused with the distance range. As the SF10 measures the time until a pulse reaches a given threshold, the upper limit is not a concern. However, the threshold must be set well over the noise level to avoid false positive detection, and then again the reflected signal amplitude must be significantly higher than the noise floor. How significant a

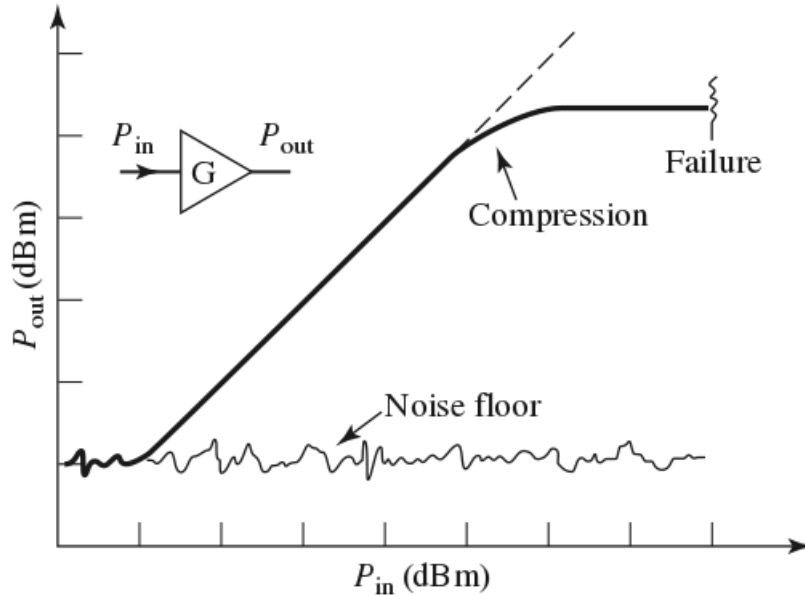


Figure 6.3: Dynamic power range of a sensor system [52, p.467]

signal is compared to noise is given by the SNR defined

$$SNR = \frac{P_{signal}}{P_{noise}}, \quad (6.2)$$

When applying the SF10 as an altimeter on an UAV, the noise sources are sunlight, fog/clouds and noise occurring inside the instrument. The SF10 radiates at 905 nm and is overlapping the spectrum of sunlight. The noise of the system will vary with environmental conditions, but also if the instrument itself accumulates heat. SNR will also be affected by the strength of the returned signal. From scattering theory, the radar equation and the radar cross section², it is clear that the signal strength will decline for low-grazing angles, long ranges and for low surface reflectivity. From the radar equation we know that the signal power will decline with a factor $1/r^4$, where r is distance to target. Together, all of the mentioned factors will define the maximum range of the altimeter.

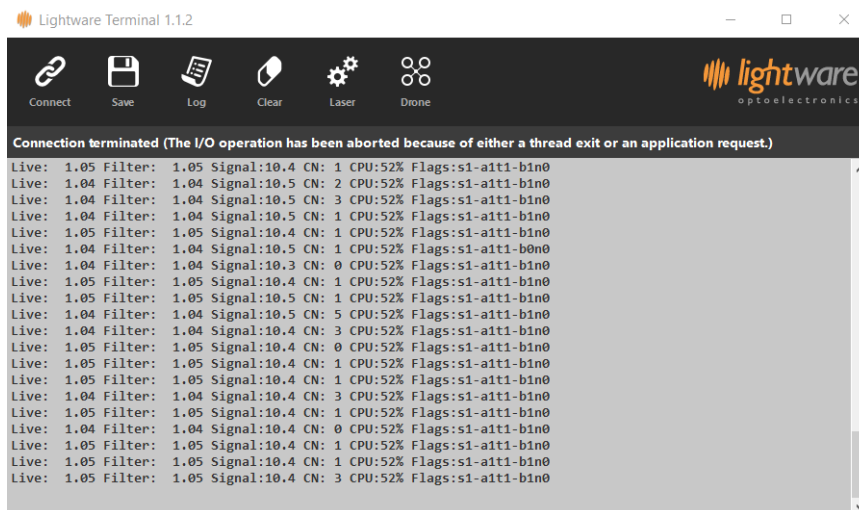
2. The radar cross section is a way to measure how well a target is detected by a radar. Most decisive factors are incident angle, polarization and wavelength of radiation and size and material of the target.

6.3 Interfacing by Lightware Terminal

The SF10 can be interfaced through both analog or digital ports (serial and I2C). Thus, it is easy to set up communication with the UAVs control system. In the work with this thesis, however, the SF10 has been connected by USB cable to a computer and Lightware Terminal (LT) 1.1.2 original software has been applied. By performing a simple "hack" the LT can reveal images of the real pulses and real-time information about the signal strength. A detailed description on how to hack the SF10 follows below and then experimental verification of how the values are obtained is presented.

6.3.1 Hacking the SF10

After the USB cable is plugged in, connecting the SF10 to LT is done by pressing the "Connect" icon in the terminal. Now, a stream of live distance readings appear in the terminal. By pressing upper case <U> and upper case <Y> you access factory functions. Pressing right arrow key and <SPACE> a new live data stream occurs (see figure 6.4), but with a bit more information. Now, in addition to the distance reading, a filtered distance read and signal strength (see section 6.5) are presented.



```

Lightware Terminal 1.1.2
Connect Save Log Clear Laser Drone
lightware
optoelectronics
Connection terminated (The I/O operation has been aborted because of either a thread exit or an application request.)
Live: 1.05 Filter: 1.05 Signal:10.4 CN: 1 CPU:52% Flags:s1-a1t1-b1n0
Live: 1.04 Filter: 1.04 Signal:10.5 CN: 2 CPU:52% Flags:s1-a1t1-b1n0
Live: 1.04 Filter: 1.04 Signal:10.5 CN: 3 CPU:52% Flags:s1-a1t1-b1n0
Live: 1.04 Filter: 1.04 Signal:10.5 CN: 1 CPU:52% Flags:s1-a1t1-b1n0
Live: 1.05 Filter: 1.05 Signal:10.4 CN: 1 CPU:52% Flags:s1-a1t1-b1n0
Live: 1.04 Filter: 1.04 Signal:10.5 CN: 1 CPU:52% Flags:s1-a1t1-b0n0
Live: 1.04 Filter: 1.04 Signal:10.3 CN: 0 CPU:52% Flags:s1-a1t1-b1n0
Live: 1.05 Filter: 1.05 Signal:10.4 CN: 1 CPU:52% Flags:s1-a1t1-b1n0
Live: 1.05 Filter: 1.05 Signal:10.5 CN: 1 CPU:52% Flags:s1-a1t1-b1n0
Live: 1.04 Filter: 1.04 Signal:10.5 CN: 5 CPU:52% Flags:s1-a1t1-b1n0
Live: 1.04 Filter: 1.04 Signal:10.4 CN: 3 CPU:52% Flags:s1-a1t1-b1n0
Live: 1.05 Filter: 1.05 Signal:10.4 CN: 0 CPU:52% Flags:s1-a1t1-b1n0
Live: 1.05 Filter: 1.05 Signal:10.4 CN: 1 CPU:52% Flags:s1-a1t1-b1n0
Live: 1.05 Filter: 1.05 Signal:10.4 CN: 1 CPU:52% Flags:s1-a1t1-b1n0
Live: 1.04 Filter: 1.04 Signal:10.4 CN: 3 CPU:52% Flags:s1-a1t1-b1n0
Live: 1.05 Filter: 1.05 Signal:10.4 CN: 1 CPU:52% Flags:s1-a1t1-b1n0
Live: 1.04 Filter: 1.04 Signal:10.4 CN: 0 CPU:52% Flags:s1-a1t1-b1n0
Live: 1.05 Filter: 1.05 Signal:10.4 CN: 1 CPU:52% Flags:s1-a1t1-b1n0
Live: 1.05 Filter: 1.05 Signal:10.4 CN: 1 CPU:52% Flags:s1-a1t1-b1n0
Live: 1.05 Filter: 1.05 Signal:10.4 CN: 3 CPU:52% Flags:s1-a1t1-b1n0

```

Figure 6.4: Lightware Terminal live output sensor data.

To dump a datafile with an image of the "real" pulses³ that make ground for the distance estimation do the following: Press <SPACE> button, press "Log"

3. The "real" pulses are not completely real as they are acquired by sequential equivalent time sampling.

icon to save file, press <D> button to dump data and press "Stop Log" icon to close the file. Now a matrix including emitted and received pulses are saved and ready for further processing and plotting.

6.4 Case Study: Range Measurements

This experiment aims to validate how the SF10 measures range to a target. It is done by moving the SF10 perpendicular to a white wall on a range from 0.5-7 m at 0.5 m step. To validate distance measurements from SF10/f, the received and transmitted pulses are recorded at every distance step. And the distance between the pulses is estimated by algorithm 1.

Algorithm 1 Thresholding Algorithm

Precondition: t and r are vectors containing transmitted and received pulses. $tresT$ and $tresS$ are user-defined and response higher than threshold is considered as a signal. As SETS corrupts the time stamps, δ is calibrated to match the true length.

```

1: function DISTANCE( $t, r, tresT, tresR$ )
2:   for  $i$  in  $t$  do
3:     if  $t(i) > tresT$  then
4:       break
5:     end if
6:   end for
7:   for  $j$  in  $r$  do
8:     if  $r(j) > tresR$  then
9:       break
10:    end if
11:  end for
12:  return  $\delta = j - i$ 
13: end function

```

The experiment gives three estimates for distance.

- The distance output from LT. Logged in vector denoted D_{LT}
- Distances estimated by implementation of algorithm 1, denoted D_I .
- Measuring tape was applied for validation, denoted D_M and referred to as true distance. Estimated uncertainty of measuring tape is $\epsilon = \pm 0.5$

cm.

In order to quantify performance the data will be normalized by elementwise subtracting the true distance from the estimated one:

$$\epsilon_{LT} = D_{LT} - D_M \quad (6.3)$$

$$\epsilon_I = D_I - D_M. \quad (6.4)$$

Now, the elements in the ϵ vectors represent the error at each distance for the two approaches. Each element in the same vector can be assumed as a realization of the same stochastic process, and thus statistical moments can be estimated. The mean is assumed to be zero, and standard deviation reduces to:

$$\sigma_{LT} = \sqrt{\frac{\sum_{i=1}^n D_{LT,i}^2}{n-1}}, \quad (6.5)$$

and equivalent for σ_I . σ will represent an average deviation from the true distance.

6.4.1 Results

The green line in figure 6.5 is a visualization of how the thresholding algorithm estimates distance. This distance is assumed to be proportional to the real distance, and a linear function is obtained for it to match the true data.

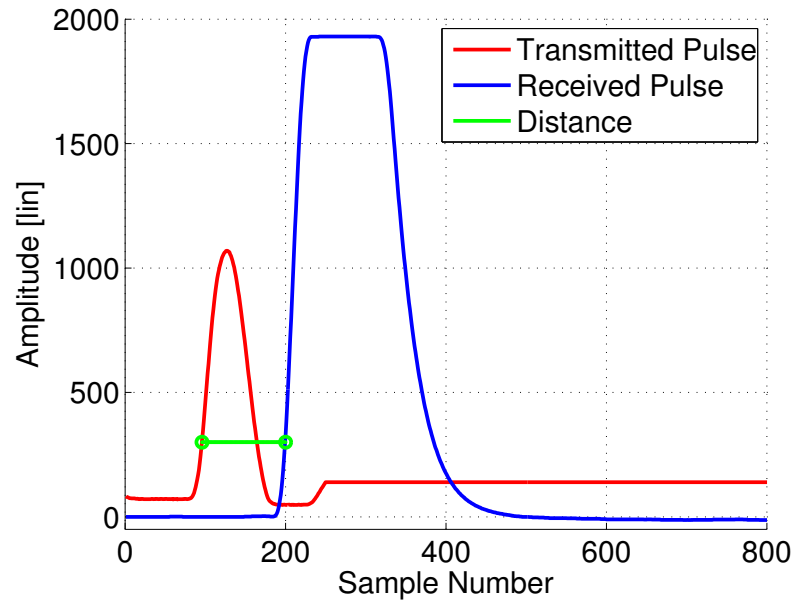


Figure 6.5: Red line is emitted pulse, blue is received. The green line shows how thresholding algorithm measures distance. Here the threshold is set to 300.

The standard deviations is computed to be

$$\sigma_{LT} = 0.3916 \text{ cm} \quad (6.6)$$

$$\sigma_I = 4.364 \text{ cm}. \quad (6.7)$$

σ_{LT} and σ_I claim that the accuracy of the LT distance about is one order of magnitude less than for the implemented threshold. This was a significant difference, without an obvious reason. Accuracy may increase if the time is measured from the trigger pulse inside the SF10 microcontroller, and from the time when the emitted pulse reaches a threshold, as it was done in this experiment. It is common to assume error probability to be normally distributed. We know that for normal distributions, $\pm 3\sigma$ covers 99.7% of the probability mass. $3\sigma_{LT} = 1.17 \text{ cm}$. This means with a large degree of that certainty the SF10 estimates distance are within $\pm 1.1175 \text{ cm}$ of the true distance. The maximal measured error was 1 cm.

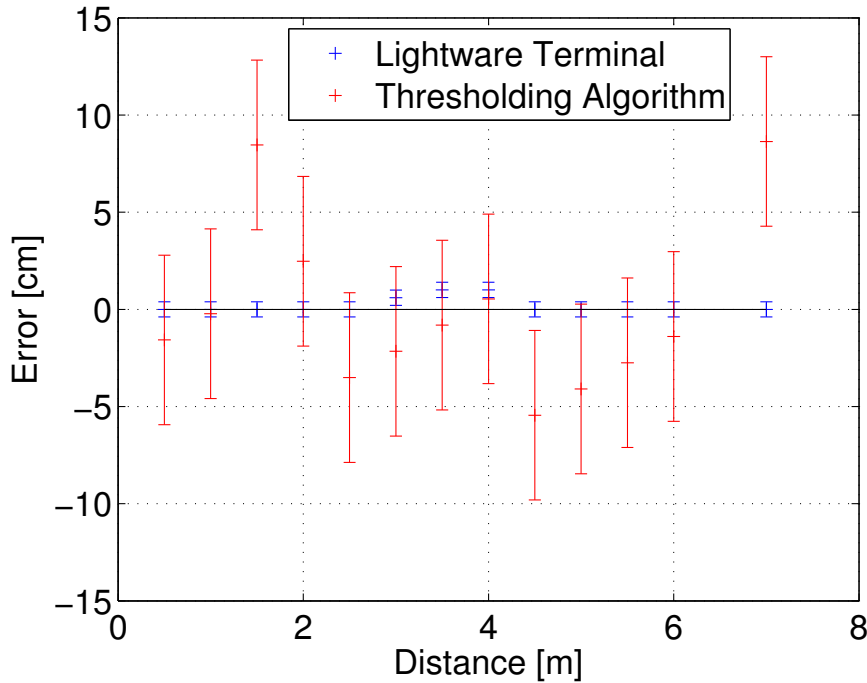


Figure 6.6: Error of the measurements at various distances with standard deviation. Blue is the distance estimated by LT and red is by thresholding algorithm. The true value is given by tape measure.

6.5 Case Study: Signal Strength Measurements

The Lightware Terminal outputs signal strength for every distance measure. To verify how this quantity is defined, both the transmitted and the received pulse were investigated, as the received pulse is a function of the transmitted power and shape. The experiment is carried out by setting up a white, shiny surface 1.00 meter from the SF10 as seen in figure 6.7. We varied the angle θ of the plate from 0 to 80° and recorded the received and transmitted pulse for every 10° . It was integrated over the whole pulse voltage V_p to obtain a signal vector $S(\theta)$

$$S(\theta) = \int V_p(t)dt, \quad \forall \theta. \quad (6.8)$$

Comparison between $S(\theta)$ with the signal strength from LT $S_{LT}(\theta)$ is done by

the correlation coefficient ρ between two vectors

$$\rho = \frac{\text{Cov}(S(\theta), S_{LT}(\theta))}{\sigma_S \sigma_{S_{LT}}}, \quad (6.9)$$

for the S and S_{LT} vector $\rho = 1$ means perfect linearly correlated, $\rho = 0$ means uncorrelated and for $\rho = -1$ they are inverse linearly correlated. The signal vectors are then applied to give a relative measure of how signal strength declines for low-grazing angles.

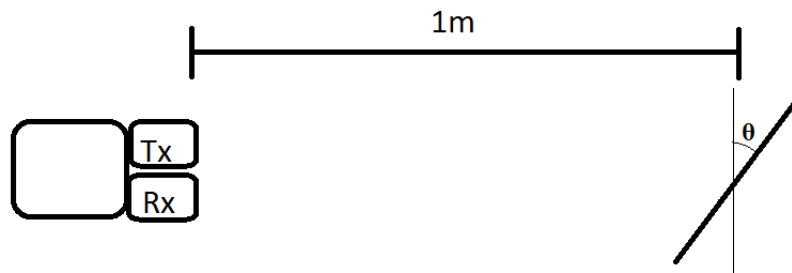


Figure 6.7: Experimental setup for signal strength measurements. The laser to the left, and the white plate to the right. θ denotes the angle between the reflection plane and the plane orthogonal to the incident radiation.

6.5.1 Results

From figure 6.8 (right), it is clear that the $S(\theta)$ for the transmitted pulses relative constant for all θ , at least compared to the received pulses in figure 6.8(left). Thus, it is only required to consider the received pulses. The signal vectors S_r and S_{LT} were then compared. For simplified visualization the curves were normalized, and it is easy to see that they are correlated from figure 6.9. The Matlab function `corr()`, which is an implementation of eq. 6.9, outputs $\rho = 0.9977$.

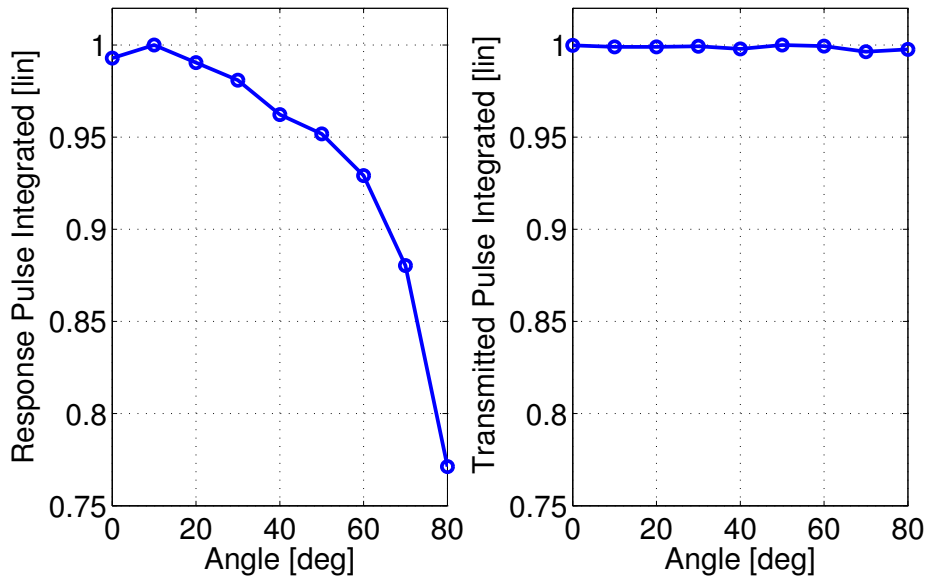


Figure 6.8: (Left) The received pulse amplitude and (Right) the emitted pulse amplitude integrated over time as a function of incident angle.

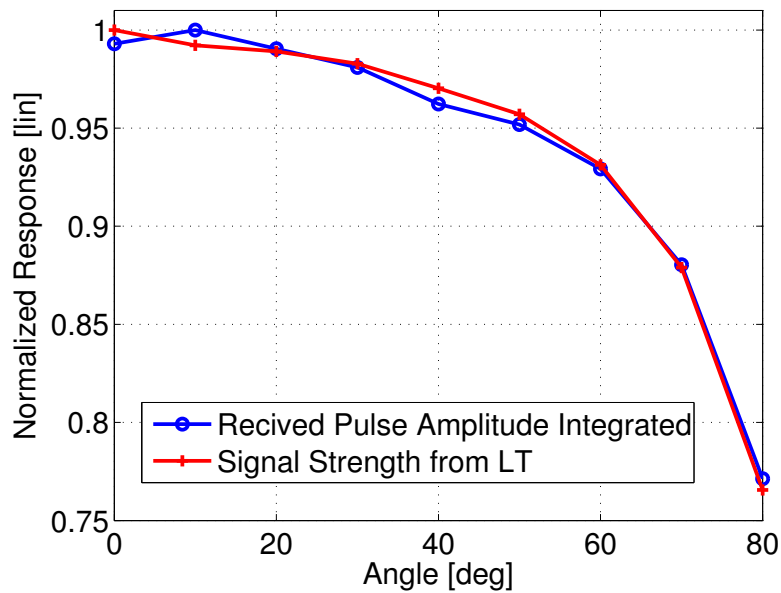


Figure 6.9: Comparison of the integrated pulses and signal strength from LT.

How the signal strength measure affects the accuracy of SF10's altitude estimation is not obvious. But, we can assume that for a strong signal, the received

pulse will have a short rise time, implying an accurate altitude estimate. To further analyse this we did a test, where the signal strength was reduced, while the SF10 was applied on a constant range. The signal reduction was performed by gradually covering the emitter and receiver with a white sheet of paper. The error versus signal strength is plotted in figure 6.10. Even though, the error is slightly increasing, as the normalized response declines, it is relative stable until the signal strength has dropped by a factor of 2.

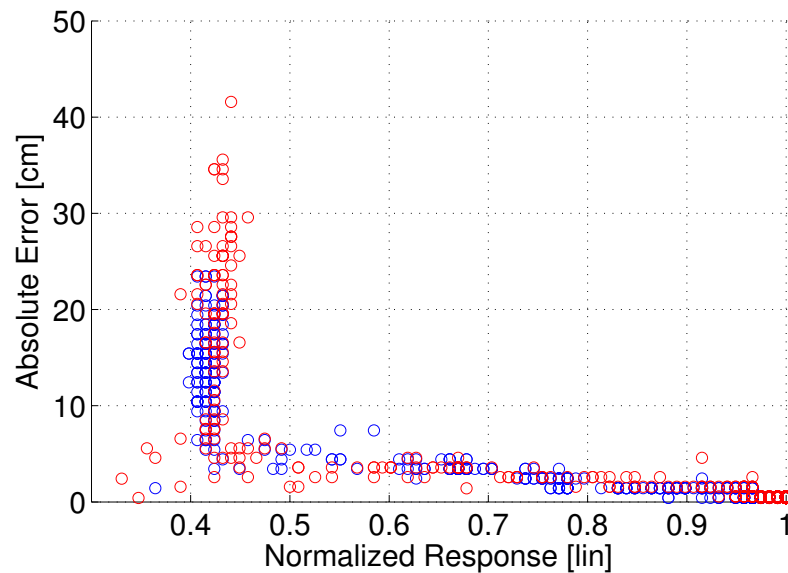


Figure 6.10: Scatter plot of the absolute error versus normalized signal strength response. The blue and red color labels refer to two independent experiments.

6.6 Safety

A laser beam can cause human hazards, given its intensity and wavelength. The SF10 (see figure 6.11) is classified as M1 safety class [34] in its datasheet. According to Rockwell Laser Industries', laser equipment classified as M1 could only cause danger if collecting optics are used [24]. Furthermore, the datasheet states that the laser beam should not be viewed using binoculars or similar on a distance less than 15 m [34].



Figure 6.11: Sticker on the SF10 claiming its safety classification [34].



Experimental Setup

This chapter will explain how the experiments are carried out in this thesis. It includes description of physical setup and the software developed for this specific purpose.

The experimental work has been a central part of this thesis. Designing and building proper platforms have been done from scratch, and several iterations have been necessary to acquire adequate data. The reflecting face, represented as the snow cover, has several features that increases the complexity of the experiments. A variety of snow conditions are likely to appear throughout the winter season, and that affects the scattering and reflective properties of the NIR radiation.

7.1 Goals of Experiments

The main aim of the experimental work is to investigate the ability of the SF10 to operate as the altimeter on an UAV during low altitude hovering over a snow covered surface. This includes applying the UAV in an array setup.

First, we wanted to investigate the performance of the SF10 on real snow conditions, by isolating decisive factors like incident angle, range and surface snow type. Then we looked into the altimeters ability to map the surface topography when sweeping over ground, simulation an UAV hovering at low

Table 7.1: Features of the stationary experiment

Range	0.5-3.5 m
Range step	0.5 m
Angle	0-80°
Angle step	10°
Snow Types	RG, SH, MF, PP

altitudes.

7.2 Stationary Experiment

From the theory part, we learned that the optical properties of seasonal snow pack in the near infrared radiation is affected by the type of snow present. Generally, results showed that through increase in grain size, the reflectivity decreased. Thus, it was of interest to present a standardized routine to a range of snow types. From the radar equation, we also know that electromagnetic radiation intensity declines as the distance to the reflector increases. Whether the reflection is specular or diffuse will also affect the back-scatter. To investigate this, we situated the altimeter at various angles and ranges, presented in table 7.1. The setup can be seen in figure 7.1.

7.3 Scanning Experiment

This measurement campaign was designed to simulate the properties of the altimeter when the UAV is hovering over ground. Hence, it was required to log data as the altimeter is on the move from an altitude of around one meter. It was obtained by mounting a rail between two ladders, as seen in figure 7.2. Specific features of the experiment is presented in table 7.2 This altitude should be verified by an independent system, with equivalent or better accuracy. It was achieved by a camera filming the cross section of the snow pack, and developing an edge detecting software. This system is thoroughly described in section 7.4.

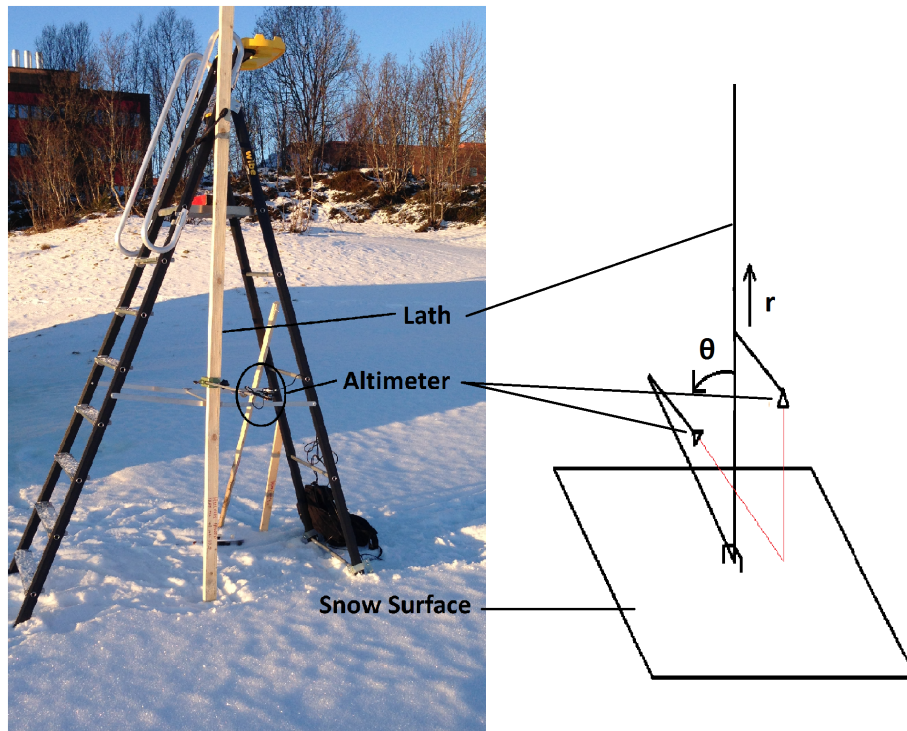


Figure 7.1: Setup for stationary experiment. (Left) The altimeter is mounted such that range r can vary. A shorter version of the wooden lath is used when the angle θ is varied.

Table 7.2: Features of the scanning experiment

Sweeping Velocity	2 cm/s
Sweeping Distance	250 cm
Height Over Ground	60-80 cm
Expected Accuracy of AEC	± 1 cm
Angle of Altimeter	$-10^\circ, 0^\circ, +10^\circ$

7.4 Altitude Estimation by Camera

To verify the altimeter data we wanted to develop a system that measures the surface topography completely independent of the altimeter. The system, referred to as altitude estimation by camera (AEC), should have at least equivalent, but preferably better, resolution than the altimeter and have the ability to scan over the snow pack. The system should also be inexpensive and not too comprehensive to implement.

7.4.1 Edge detection

In the field of digital image processing, edge detection techniques are used for sharpening images. To detect edges the gradient operator is applied to the image function I [19]:

$$\nabla I = \frac{\partial I(x,y)}{\partial x} + \frac{\partial I(x,y)}{\partial y} \quad (7.1)$$

The motivation for using edge detection in this specific application is to detect the snow surface in an image of the cross section. In the picture frames obtained there may be transitions in the snowpack and background elements like trees, in addition to the snow surface, that represent rapid transitions in pixel value, and thus they can be detected as edges. Such edges are referred to as false edges, and if they are found to be the most prominent edge in the picture, this is manually taken hand of.

7.4.2 Image Smoothing

As the resolution of the video frames are relative high compared to the required accuracy, we can afford to blur the image slightly. This is performed to reduce the risk of small, rapid changes in intensities in the image should appear as the most prominent edge. Such edges could be caused by e.g. shadows or ice particles that naturally appear in this environment. The smoothing is performed by convolute the image with a mask [19]:

$$w(x,y) = \frac{1}{9} \begin{bmatrix} 1 & 1 & 1 \\ 1 & 1 & 1 \\ 1 & 1 & 1 \end{bmatrix}. \quad (7.2)$$

By convoluting the mask $w(x,y)$ and the original image, a smoothed image $S(x,y)$ can be obtained by:

$$S(x,y) = w(x,y) \star I(x,y) \quad (7.3)$$

Convolution operator is denoted \star .

7.4.3 Model Physical Altitude from Image

A digital camera measures the incoming light from a range of different angles, and projects it onto a 2D surface, called a photo. Thus the objects near the edges of a photo, will be more stretched, with lower resolution, than in the middle of the same photo. This effect can be neglected in most contexts, but when a photo is applied for high accuracy proximity measures, it needs to be

considered. This is achieved by creating a model of the relationship between deviation from the center pixel of the image, and the physical dimension of a pixel. In the work with this thesis, we found the relation between edge pixel and physical height of the snow surface from picture frames containing a ruler that proved distance references.

7.4.4 Digital Camera

To find a proper camera for this application some criteria were set. It should be robust, water resistant and able to film with good enough resolution. The latter is fulfilled if accuracy of the surface topography is estimated well beyond the accuracy of the SF10, which is 1 centimeter. Features of the chosen camera can be seen in 7.3

Table 7.3: The camera model applied for surface mapping with its relevant attributes when executing the experiment.

Model	Olympus Tough 6010
Mode	Video - VGA
Pixel Resolution	480 x 640 pixels
Spatial Resolution	1 mm/pixel at 50 cm range
Frequency	15 frames per second

7.4.5 Altitude Estimation by Camera Algorithm

An algorithm with several steps is developed to estimate the height of the snow surface.

1. Transform RGB image to an 8 bit grayscale image by Matlab function `rgb2gray()`. All pixel values are now represented by an integer between 0 and 255.
2. Extract the vertical column of pixels in the middle of the image, represented by the matrix I , with elements $i_{j,k}$

$$I = \begin{pmatrix} i_{1,1} & i_{1,2} & i_{1,3} & \dots & i_{1,n/2-1} & \boxed{i_{1,n/2}} & i_{1,n/2+1} & \dots & i_{1,n} \\ i_{2,1} & i_{2,2} & i_{2,3} & \dots & i_{2,n/2-1} & \boxed{i_{2,n/2}} & i_{2,n/2+1} & \dots & i_{2,n} \\ \dots & \dots & \dots & \dots & \dots & \dots & \dots & \dots & \dots \\ i_{m,1} & i_{m,2} & i_{m,3} & \dots & i_{m,n/2-1} & \boxed{i_{m,n/2}} & i_{m,n/2+1} & \dots & i_{m,n} \end{pmatrix}$$

3. Apply a low pass running average filter to reduce noise and probability

of false edges.

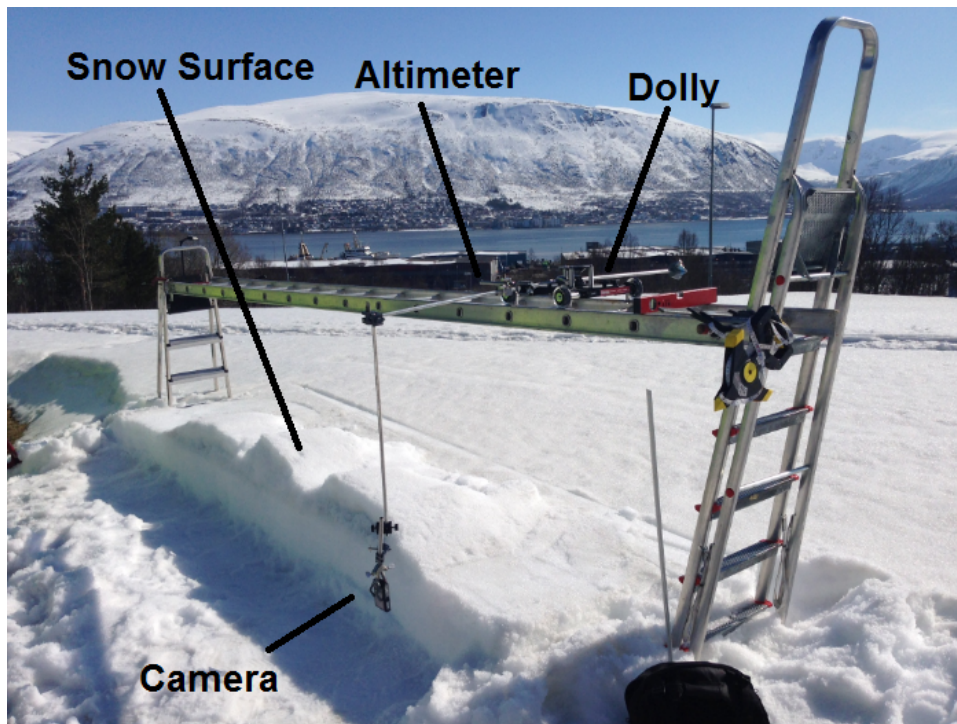
$$I'_{smooth} = [i_{1,n/2} \quad i_{2,n/2} \quad \dots \quad i_{m,n/2}] \star [1 \quad 1 \quad 1 \quad 1]. \quad (7.4)$$

4. Find the gradient of this vector by Matlab function `gradient()`. The gradient vector reveals where the most rapid changes of intensity, or edges, are located.
5. As we assume the snow surface to be continuous, a more robust way to detect the snow surface was achieved by narrowing the scope of where to look for the edge. By only evaluating ± 15 pixels (± 1 cm) the probability of detecting false edges decreased significantly. This requires knowledge of where the edge is located in the first frame of the video.
6. A model, as described in subsection 7.4.3 is developed to determine the physical height of the edge pixel.
7. Result smoothed by a running average filter of 5 pixels length.

7.4.6 Parameters

Two parameters are required for the algorithm to work properly. First, it is necessary to define a scope of where to look for a new edge point. This scope was set to 15 pixels, or about a centimeter in physical height. A larger scope would increase probability of false edges lying nearby to be detected, with a more narrow scope the algorithm would not be dynamic enough at rapid changes in the surface height. The adaptive approach reduced the probability of detecting false edges significantly, but the algorithm still lost track of the surface at some points ($< 0.01\%$), this was solved by a brute force approach where the surface height was manually set back to where the surface appeared to be.

When developing an algorithm, it is often preferable to avoid user-defined parameters. Need of parameters will make the algorithm less general, and may allow the user to tweak the result in his favor. The obvious aim of this study, is for the height mapping by camera to correlate well with the altimeter data. Thus, the parameters were set before the AEC height data was compared to altimeter data.



(a)



(b)

Figure 7.2: (a) Setup with camera and altimeter ready to sweep leftward over the surface and (b) one picture frame from the camera. The red cross shows where the snow surface is estimated to be.

/ 8

***In situ* measurements**

Along with the laser altimeter measurements, several features of the snow pack were collected. This chapter will give a brief insight in how grain size and shape, hardness, temperature and humidity are determined, all very common methods in the snow science community [70].

8.1 Grain Size and Shape

As table 4.1 states, grain size can vary from a tenth of a millimeter to more than five millimeters. It is also found to be related to the reflective properties of NIR radiation.

To measure the exact grain size *in situ* can be challenging for new dry snow, as the mean grain diameters can be around 1 mm. Small structures that are hard to measure exactly. The grains size and shape were found by inspecting them through a magnifying loupe on a crystal study board, as seen in figure 8.1.

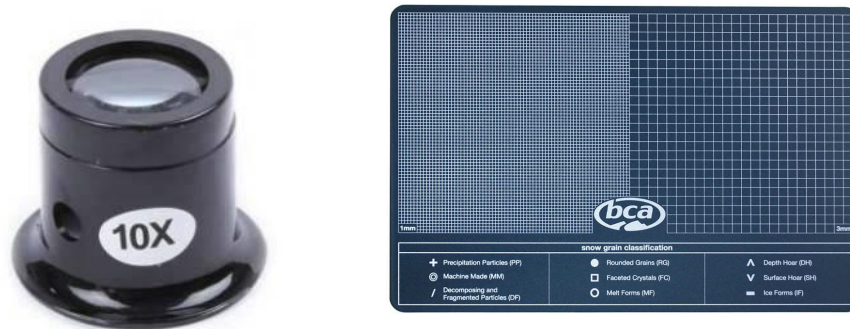


Figure 8.1: (left) A ten times magnifying loupe. (right) Polycarbonate Crystal Card delivered by the manufacturer BCA. It has 1 and 3 mm grids, designed for *in situ* study and classification of snow crystals [6].

8.2 Hardness

The most common *in situ* assessment of hardness of deposited snow is done by the "hand test". This test is carried out by digging a snow pit, so that you get access to the vertical profile of the snow pack. Then, the observer gently tries to penetrate the snow with his fist, four fingers, one finger and so on until it goes through [18, 70]. See table 8.1 for the full procedure. The snow pack often has a heterogeneous vertical distribution and this test must be made for all the different layers.

Table 8.1: *In situ* measurements of hardness of snow [18]

Term	Hand Test
very soft	fist
soft	4 fingers
medium	1 finger
hard	pencil
very hard	knife blade
ice	ice

8.3 Temperature and Humidity

Air and snow temperature and humidity are collected as it is important factors affecting the metamorphism of snow. Snow temperature is measured near the surface of the snow with a digital thermometer with resolution of 0.1°C . Air

temperature and relative humidity is collected from the weather station of the Institute of Computer Science of UiT the Arctic University of Norway [25], which is located nearby the site where experiments were carried out.

Part III

Results

/9

Stationary Experiment

This section will present the results of the stationary experiments. The stationary experiment was performed by varying the angle and distance from the SF10 laser altimeter to the snow cover as described in table 7.1. The routine was done three times, in order to minimize the error caused by inaccurate adjusting of height and angle. Moreover, 150 data points were collected at every measurement, which took about 5 seconds to record. For comparison, measurements were done at a range of snow conditions, outlined in table 9.1.

First, a thorough description of the snow conditions that occurred during the measurement campaign follows, then the measurement results will be presented.

9.1 Snow Conditions

Table 9.1: Overview of snow conditions during the measurement campaign. The most typical surface grains, namely rounded grains (RG), melt forms (MF), surface hoar (SG) and precipitation particles (PP), all occurred.

Date	Air/Snow[°C]	Humidity[%]	Grain Type	Grain size[mm]	Hardness
January 24th	-4.7/-2.5	53 %	RG	0.5	F
January 27th	6.0 /	70%	MF	5	1F
February 9th	-4.9 / -6.8	76%	SH, RG	5-10, 2	F
February 9th	-4.9 / -6.8	76%	SH, RG	3-8, 2	F
February 22nd	-5.0/-4.8	72%	PP	0.5-3	F

January 24th

Two days since last snow fall. The precipitation particles have metamorphosed into rounded small grains. Snow appears light, dry and soft during the measurements, as has not been subject for wet metamorphism, since accumulated.

January 27th

A period of warm and rainy weather made the snow pack wet and the grains are large and near-spherical. As see in figure figure 9.2, the grains are melting together.

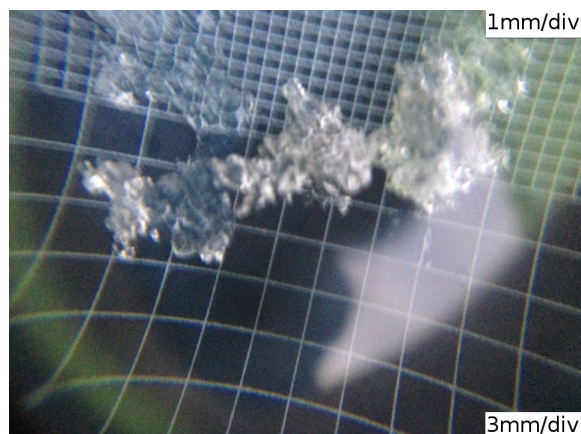


Figure 9.1: During a warm period, wet metamorphosis made large melt forms of 5 - 10 mm. Collected January 27.

February 9th

Before the measurements it was a period of cold, but humid condition (daytime around -5°C , night -9°C , 76% humidity¹) and the snow pack was shallow (30 cm). As we learned in section 4.1, this can result in surface hoar. The layer of large grains was 5-10 mm (see figure 9.2(right)), and covered a layer of much smaller rounded grains. There were large local differences in the size of the surface hoar, and for comparison, we also measured surface hoar grains of 3-8 mm this day.

February 22nd

Surface covered by light dense newly fallen snow. Even though the rounding process has started, fragmented precipitation particles were the most prominent grain type. Typical precipitation grains like stellar dendrites, needles and plates were easy to recognize with the 10x magnifying loupe (see figure 9.2 (left)).

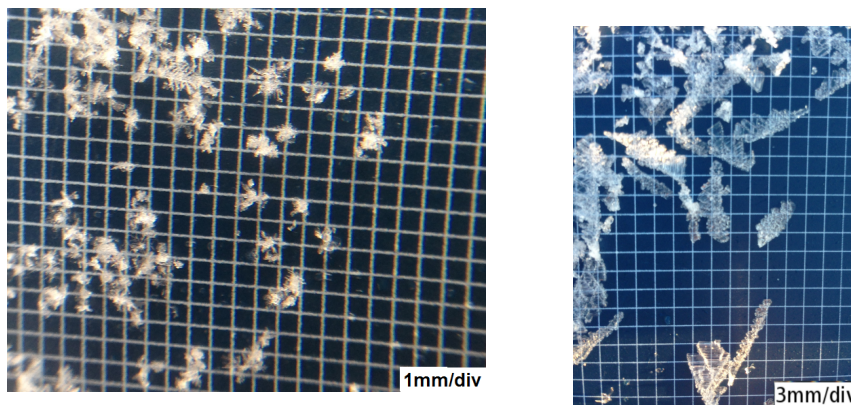


Figure 9.2: (left) Precipitation particles of size of around 1mm. (right) Large surface hoar crystals 10-20 mm. Note that the grid resolution is 1 mm for (left) and 3 mm for (right)

9.2 Results

The data was collected by fixing the SF10 sensor at various heights and angles relative to the snow surface. Every given distance and angle are reset three times, to reduce the error due to slight misplaced sensor. The sensor recorded

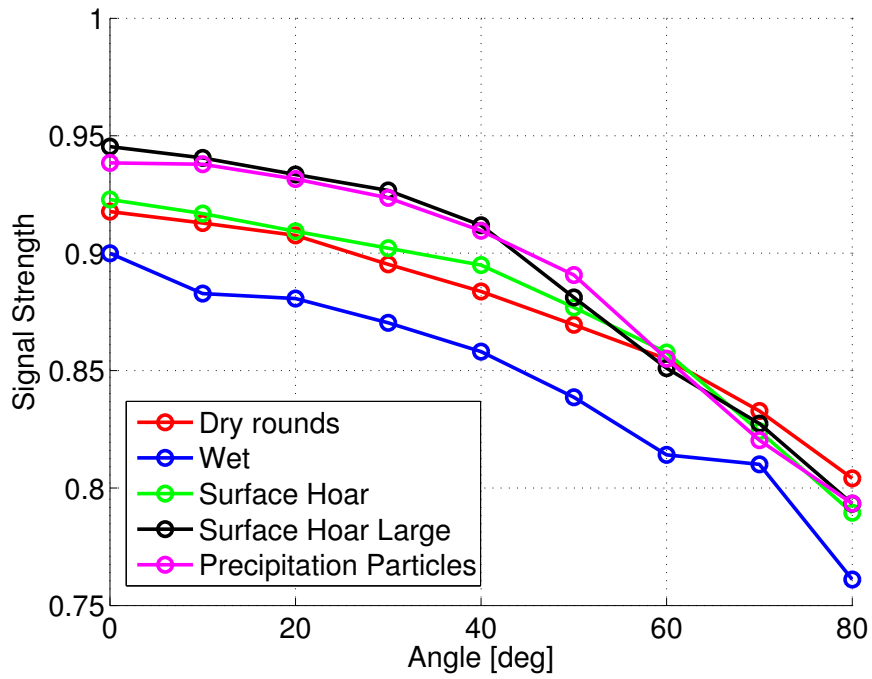
1. https://www.yr.no/sted/Norge/Troms/Tromso/Tromso/detaljert_statistikk.html

for 5 seconds, or 150 data points, for every distance and angle. Hence, 450 data points were averaged, and make up the points plotted in figure 9.3 and 9.4. The measurements are presented below related to the grain characteristics and not the date. To sum up, at January 24th dry rounds were collected, January 27th wet snow, February 9th surface hoar and large surface hoar and February 22 precipitation particles.

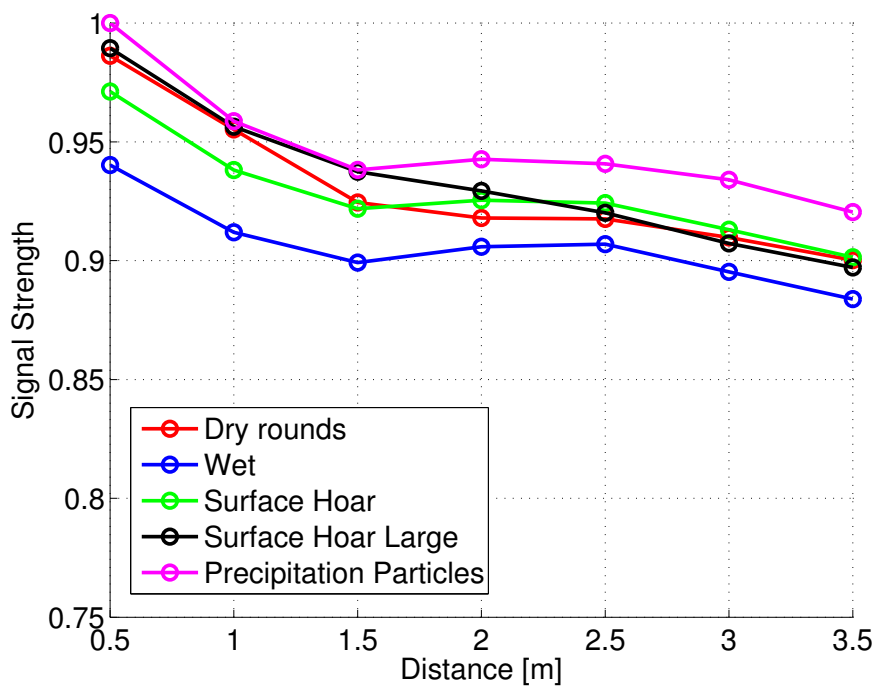
To investigate how robust the SF10 is to deviations in the UAVs altitude and attitude the signal strength (SS) is considered in figure 9.3. SS is reduced by 7% going from 0.5 to 3.5 meters range, see figure 9.3a. It is reduced 16% from 0 - 80° incident angle, but only 4% reduction from 0 - 40°, see figure 9.3b. Thus, low altitudes and moderate fluctuations in pitch and roll, will only have a marginal effect on the received signal strength.

During the measurement campaign, the distance read (DR) from the SF10 was logged three times for 5 seconds, as described over. The DR was then averaged and normalized due to the reference distance, before plotted in figure 9.4. The average deviation from true values is calculated and displayed in table 9.2. The figure and table states that wet snow has the highest error rate, with a root mean square (RMS) error of 2.81 cm. Largest measured error for wet snow error is 4.3 cm. Even if the routine was performed three times, around ± 1 cm measurement error was expected as the physical setup contained several joints and angles that may reduce the accuracy.

The most prominent result from comparing five different snow types, is that wet snow has the least energy reflected. This is true for every angle and distance and the range estimates were also least accurate on wet snow. Even though surface hoar grains appeared as the largest on the BCA board, it had a small average radius compared to wet snow. Surface hoar is a near-2D structure, like a leaf. Wet snow, on the other hand, appears as sphere-like grains, often melted together. Optical grain size is found by averaging over three dimensions, and then wet snow has the largest grain size. However, even for wet snow the signal is strong at the considered angles and ranges.



(a)

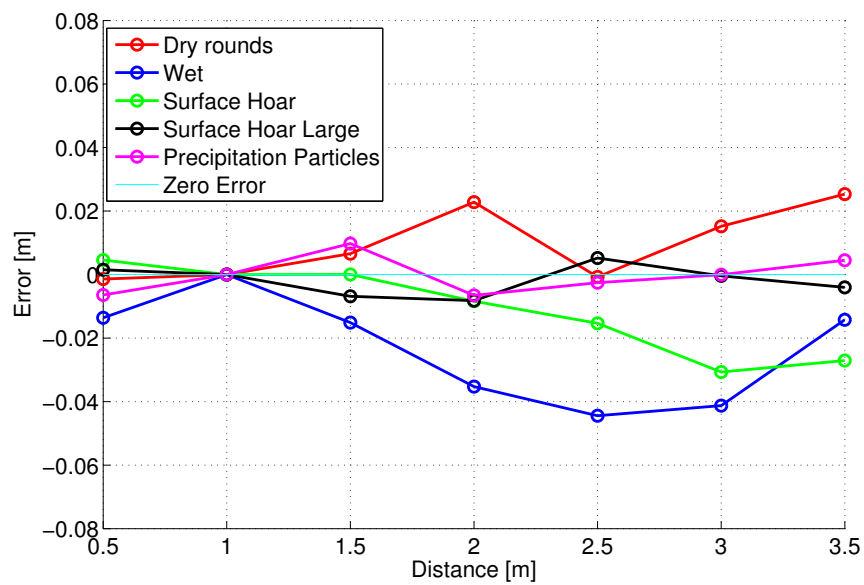


(b)

Figure 9.3: Signal Strength of returning signal when varying angle (a) and range (b) at various snow conditions.

Table 9.2: RMS error of the measurements presented in figure 9.4 for the different snow types.

Date	Snow Type	RMS error [cm]
January 24th	Dry rounds	1.43
January 27th	Wet	2.81
February 9th	Surface Hoar	1.69
February 9th	Surface Hoar Large	0.48
February 22nd	Precipitation Particles	0.54

**Figure 9.4:** Error in range measurements from 0.5-3.5 m at various snow conditions. The values are an average of the deviation from the true distance read (cyan). Also normalized at 1 m.

/10

Scanning Experiment

In the scanning experiment, the altitude is estimated by two independent sources, the SF10 laser altimeter and by camera. Thus, this section is mainly a study of their correlation. The AEC algorithm was explained thoroughly in section 7.4.5, and in figure 10.1 it is shown how a vertical column from every frame in the film is merged together to an image of the cross-section of the snow pit. The red line in this figure shows where the edge is estimated to be with the AEC algorithm. An interpretation of figure 10.1 indicates that the red line follows the edge of the snow, and that the AEC have sufficient accuracy.

A visual comparison of the AEC data against altimeter data is presented in figure 10.2. A quantitative approach is also done to investigate their correlation. Estimated mean error μ and RMS error are presented in table 10.1, and shows mean error to be about 0.25 cm with standard deviation 1.7 cm for the unfiltered altimeter data. The estimated mean error not is very interesting, as it could be removed by calibration. A slight improvement is achieved by smoothing the altimeter data with a running average filter, which is also shown in the table for filters of length 5 and 21. If such a filter is applied in a real time system, it will cause a delay proportional to the length of the filter. In figure 10.3, the absolute error is visualized. The error is smallest from 0-150 cm, where the topography is smoothest. This was expected, as it was easiest to make the top of the snow pit flat in these area. If the snow pit top was not flat where the edge was detected by AEC, then the spot illuminated by the SF10 will no be at the same level, and it will contribute to the error. A rough estimate for this is ± 1 cm.

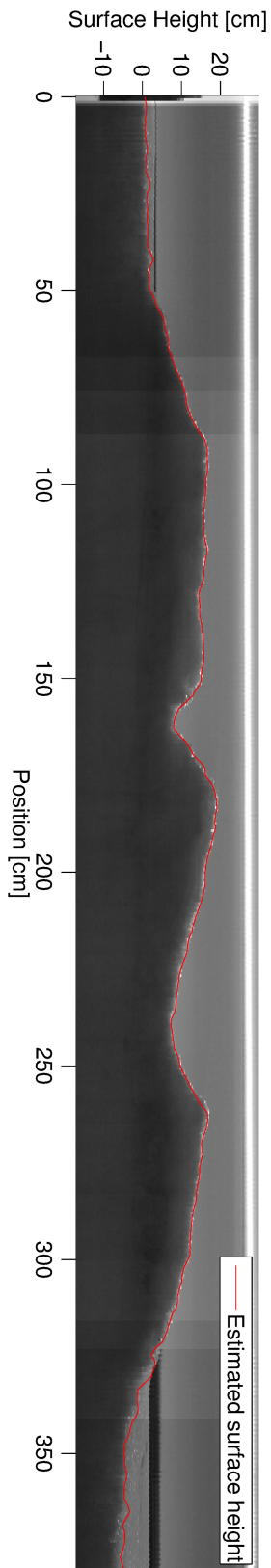


Figure 10.1: An image of the cross section of the snow pit with equal scaling of the axes. The image is a merging of one pixel columns from over 500 frames recorded as the camera traversed along the snow pack. The red line shows where the edge of the snow is estimated to be, and make grounds for the altitude estimation by camera.

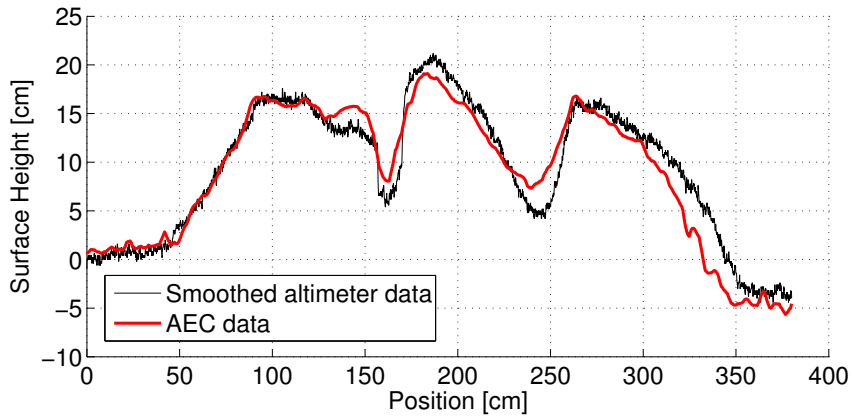


Figure 10.2: Comparison of height data generated by AEC (red) and SF10 altimeter data smoothed by running average of length 5 (black).

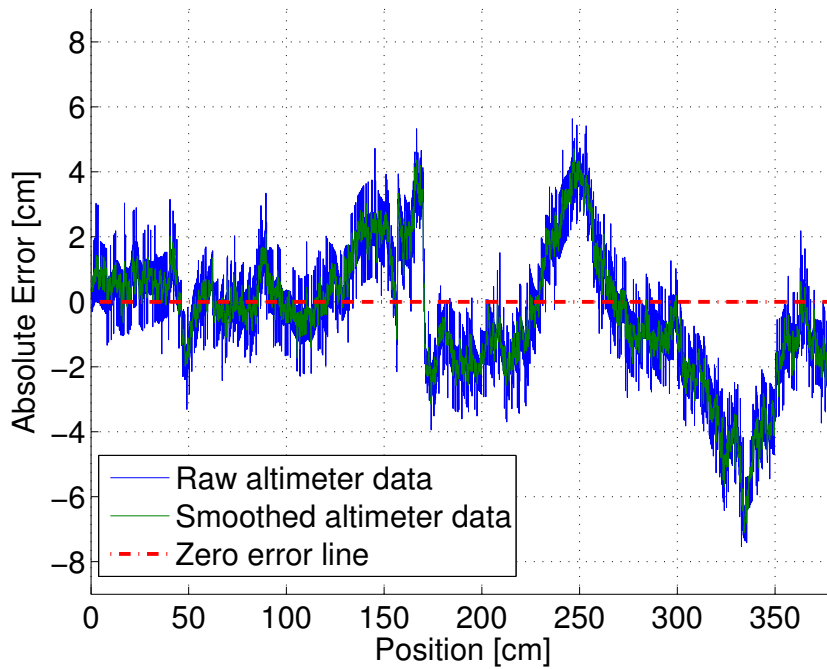


Figure 10.3: Error of SF10 altimeter data compared to AEC data.

Table 10.1: Quantitative comparison of AEC data with SF10 data. μ denotes the mean error.

Condition	μ [cm]	RMS [cm]
Unfiltered data	0.2465	1.6881
Running average size 5	0.2466	1.5654
Running average size 21	0.2468	1.5331

10.1 Array

In the scanning experiment, the array approach presented in section 3.3.2 was also conducted. To simulate an UAV with two altimeters mounted with 20° angle along the scanning direction, we directed the SF10 altimeter 10° backwards first and then 10° forward along the rail direction. Then it traversed the snow surface, similar to how it was done above, where the SF10 was directed downwards. The data from this experiment is presented in figure 10.4. The altitude recorded by backward and forward facing altimeters appears as shifted versions of each other, both overestimating the altitude compared to the downward, as expected.

By equation (3.11) the altitude can be found, based on data from backwards and forward facing altimeters. This altitude is in figure 10.5 presented alongside data from the downward facing altimeter. An estimation of the surface height from the backward and forward facing altimeters is presented alongside the height estimations from the downward facing altimeter in figure 10.5. The first 120 and last 100 cm, the altitude estimations appears to be within ± 2 cm, compared to the downwards facing altimeter. Between 120 and 280 cm, as the surface topography varies more, and the error is generally significantly larger.

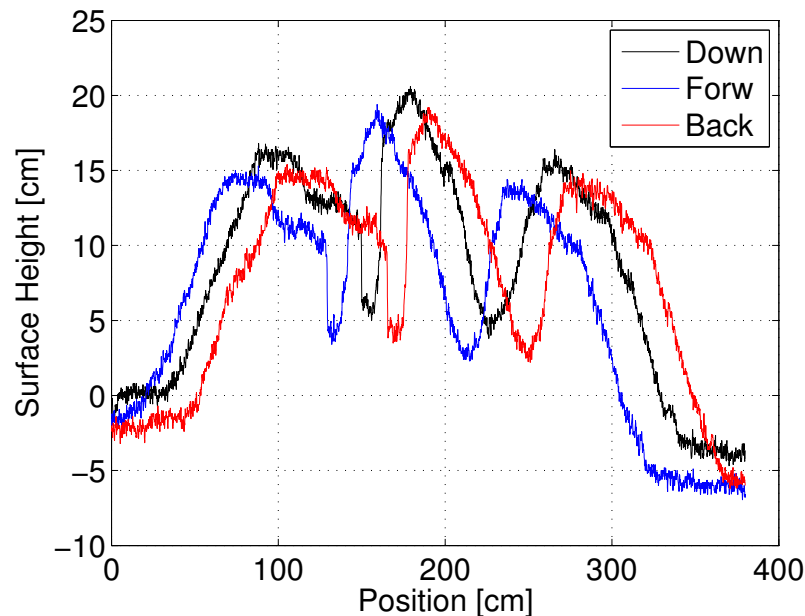


Figure 10.4: Data recorded with the SF10 altimeter directed 10° forward (blue), 10° backward (red) and downward (black).

In section 3.3.2 it was also derived an algorithm for calculating the tilt angle

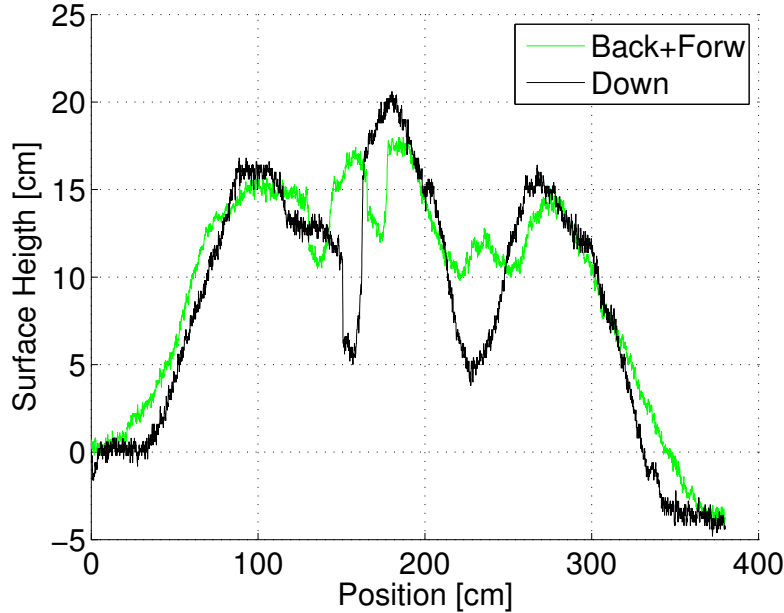


Figure 10.5: Height data from downward facing SF10 altimeter (black) and calculated height data from backward and forward directed SF10 altimeters (green).

of the surface from a forward and a backward facing altimeter, as well as a downward and forward facing altimeter. We applied the data plotted in figure 10.4 and calculated the surface slope angle in both cases. For comparison, we obtained a reference surface tilt from the downward facing altimeter. This was done by firstly smoothing the data, then finding the numerical gradient by Matlab function `gradient()` from the smoothed altimeter data denoted $a(x)$, where x is the position across the snowpack. Then the surface tilt was found by:

$$\phi(x) = \arctan\left(\frac{da(x)}{dx}\right). \quad (10.1)$$

Note that this method fundamentally differ from how the surface tilt found by the array approach. By derivation, it was not necessary to assume the surface to be flat, thus the method is expected to be more accurate, especially in the areas with large surface curvature.

From figure 10.6 it is clear in the part where the surface topography is very bumpy (from position 120-280 cm) down- and forward altimeters are closer to the downward than the back- and forward. In table 10.2, surface tilt angle estimations by the three methods are presented. Taken this into account, both setups appear to estimate the angle within $\pm 2^\circ$ at the relative smooth part of the slope (position 0-120 cm and 280-380 cm).

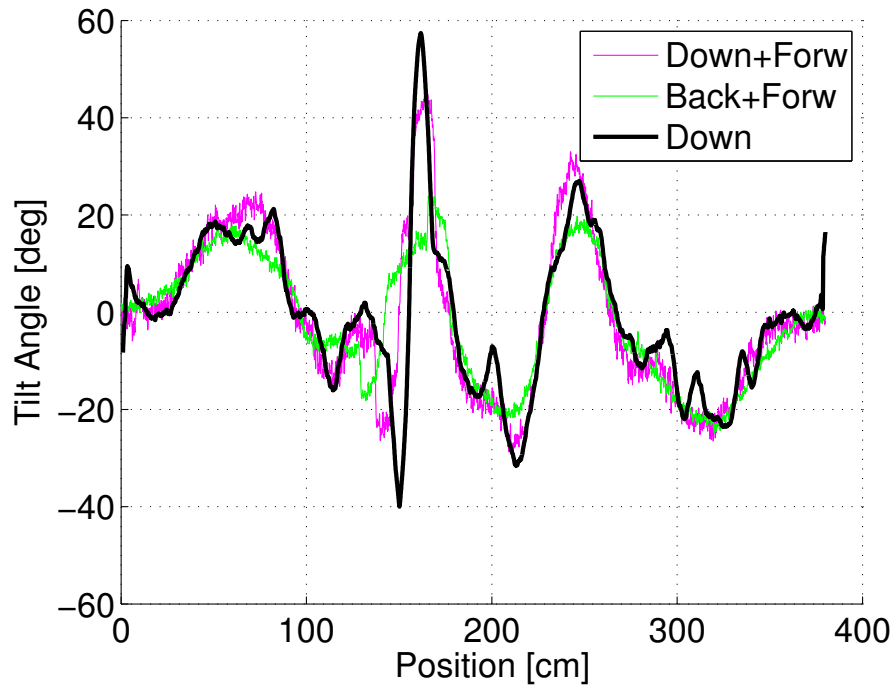


Figure 10.6: Slope angle calculated from downward facing altimeter by equation (10.1) (black) compared to the angle obtained by the forward and backward facing (green) and by the downward and forward facing altimeter (magenta).

Table 10.2: Estimated surface tilt at position 1 (10 cm) and position 2 (65 cm) along the horizontal axis. Altitude estimation where carried out with following setups; downward, forward+backward and downward+forward facing altimeters.

Method	Surface Tilt 1 [deg]	Surface Tilt 2 [deg]
Downward	0	18
Forw + Back	1	18
Down + Forw	0	20

/ 11

Complementary Results

The results presented in the previous chapters are aiming to investigate the main concerns for applying the SF10 as altimeter for a low altitude hovering UAV over a snow surface. This chapter, presents complementary experimental results, describing properties of the SF10 altimeter of interest for future adaptation in UAVs.

11.1 Long Ranges

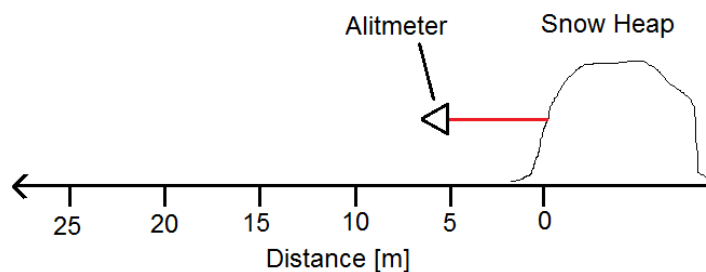


Figure 11.1: Experimental setup when applying the SF10 altimeter on long ranges from a snow heap.

Even though the main operational range for the UWibaSS is set to < 6 m [26], an experiment to validate the SF10 altimeter abilities on longer ranges were carried out. For navigation purposes, knowing the exact altitude of the UAV can be of interest even though the UWibaSS is not operating. The setup was simple; a large snow heap was the reflective surface, and the sensor were moved along a tape measure for reference, as seen in figure 11.1. Distance and signal strength were logged at 5 to 40 m with 5 m steps. Above 40 m the signal disappeared.

The maximum range of the SF10 is given to be 25 m i the manual [34], but from figure 11.2(left) it is clear that th signal occurred until 35 m, and it disappears when approaching 40 meters. However, the accuracy seemed to decrease significantly above 25 m. Above 25 m the SS was reduced to $\sim 50\%$, as seen in 11.2(right). Range measurements displayed are averaged over 100 data points, and the size of th errorbars in figure 11.1 are representing the standard deviation estimated based on this 100 sample. At 35 m, the range estimations are fluctuating at a high rate. It must be emphasized that the experimental setup were unsophisticated, and uncertainty of around 20 cm was expected. The result shows that the SF10 altimeter has an operational range well beyond the required distance of 6 m, and that it will provide the UAV with relative accurate altitude estimations up to at least 25 m.

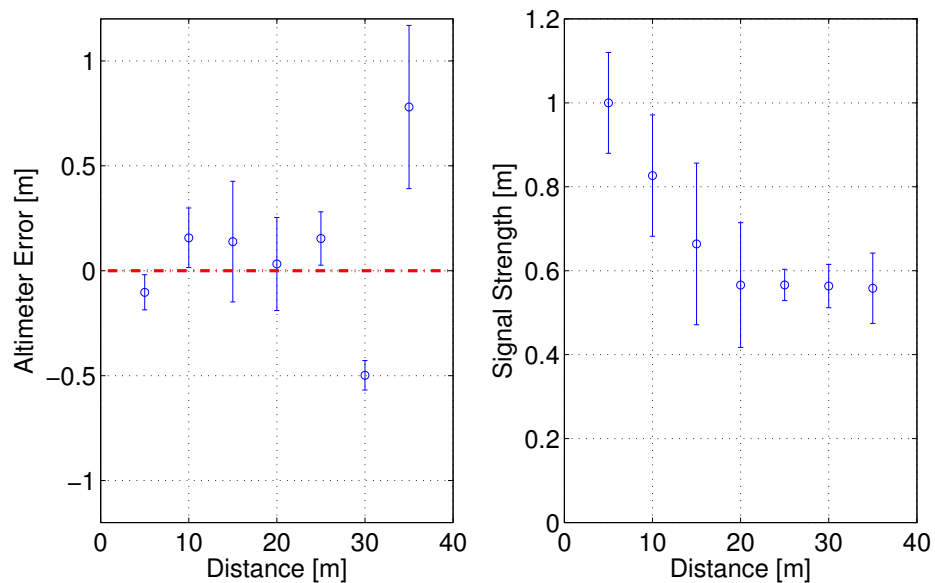


Figure 11.2: (Left) Averaged range measurements by the SF10 altimeter vs the true distance to a snow surface. (Right) Corresponding averaged signal strength measurements with errorbars.

11.2 Crosstalk

The array setup that is proposed in this thesis, is based on a setup with multiple altimeters recording simultaneously, hence it is required to consider the possibility of crosstalk between several sensors operating simultaneously. Crosstalk occurs if radiation from one of the sensors is picked up by an other sensor and disrupting its signal. For optical radiation it is possible to focus the beam, to produce close to a pencil beam radiation pattern, which reduces the risk of crosstalk. The SF10 laser beam has a divergence angle of only 0.4° . To investigate crosstalk issues, the SF10 altimeter logged the range to a white surface. While it was recording, a similar altimeter operating on the same frequency where pointed at the same direction simulating a worst case scenario, as seen in figure 11.3. Later the angle between the laser beams were set to 10° , and at last only the SF10 where present as a reference.

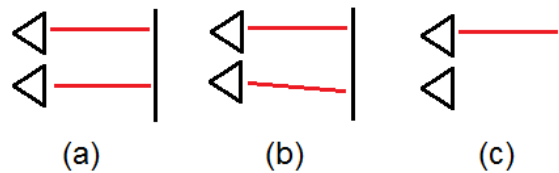


Figure 11.3: Setup for crosstalk experiment. (a) Applying two aligned altimeters, (b) two altimeters with divergence angle of 10° between the beams and (c) only one altimeter for reference on a range of 1 m.

Table 11.1: Results from studying data recorded from a SF10 altimeter set up with a similar altimeter aligned, with 10° divergence between beams and just one altimeter for reference. Outliers are values that deviated more than 2 cm from the estimated mean value, including not available values. When estimating RMS error for aligned sensors, not available values were removed, which accounted for 0.0967% of the values.

Setup	Outliers	RMS error
Aligned sensors	0.86%	0.0169 cm
10° angle	0.00%	0.0050 cm
Only one sensor	0.00%	0.0049 cm

Results presented in table 11.1 showed that, for the worst case scenario, less than 1% of the recorded values had an error of more than 2 cm, when applied on 1 m range. For the case of 10° divergence between beams, it was no significant difference from the reference case were only one sensor recorded. Hence, crosstalk appears to have no significant influence on the data, if sensors is mounted with a 10° angle.

Part IV

/12

Suggestion to Implementation of Array Setup

Based on the results in the previous chapters, we will in this section suggest how to implement the array of altimeters setup.

12.1 Physical Setup

There are several variables to consider when designing the physical setup of the altimeter array, to derive distance and local tilt angle of the terrain. Most prominent is how many sensors are needed, and where to direct them. Limitations in direction is mainly due to how large area on the surface that is assumed to be flat. As an example, if the UAV in figure 12.1(right) hovers 2 meter over ground and have a θ angle of 20° the laser spots on the ground would be 71 cm apart, thus, for the height estimation to be correct it should be flat between these two spots. On the other hand, if the distance between the spots are to small, it may pick up small scale roughness on the surface. A snow surface can have ripples like on a sea surface, and this will appear as noise in the search of large scale surface tilt. This phenomena is visualized in figure 13.1

It is also important to consider the reflection properties for the given radiation at a snow surface. This is measured and plotted in figure 9.3a. The result showed that the reflection is very diffuse, implying that the signal strength will maintain detectable even at low-grazing incident angles.

We will, based of the mentioned considerations, recommend the setup displayed in figure 12.2, that is a 3D version of figure 12.1 (left). Note that these figures illustrate a surface aligned with the UAV, see figure 3.2 (left) at page 26 for the general case with the surface tilted an angle ϕ relative to the UAV. The downward facing laser will ensure that the height estimation is robust regardless of the surface. Further, the forward and sideways facing altimeter, together with the downward, provide estimation of the tilt angle of the surface. It can aid height estimation.

Angle θ in this setup may be about 10° for an operational height of 1 to 5 meters. The distance between the spots will be correspondingly 18 to 88 cm. Crosstalk between the sensors will evidently be of no concern, according to table 11.1.

The physical arrangement for the array setup in the 2D case for both case 1: downward and forward facing altimeters, and case 2: forward and backward facing altimeters, is presented in section 3.3.2 on page 25. The setup is presented with an arbitrary surface tilt ϕ , and equations for resolving altitude and surface tilt is derived. The nomenclature presented here in this section is consistent with section 3.3.2, which is presented in table 3.1.

In figure 12.1, the perfectly aligned situation is presented for case 1 (left) and case 2 (right). The equivalent aligned situation can be found in figure 12.2, which is the 3D version of case 1. The conditions for assuming the UAV so be aligned with the surface is given by:

$$d_p = d_r = \frac{h}{\cos\theta}. \quad (12.1)$$

Hence, we can from this derive the error in pitch ϵ_p and roll ϵ_r angle correspondingly by:

$$\epsilon_p = d_p - \frac{h}{\cos\theta} \quad (12.2)$$

$$\epsilon_r = d_r - \frac{h}{\cos\theta}. \quad (12.3)$$

In stead of deriving the surface tilt on the fly, the control system of the UAV can take the error-values ϵ_p and ϵ_r into its proportional-integral-derivative (PID) feedback loop, and by that controlling the UWibaSS radar beam.

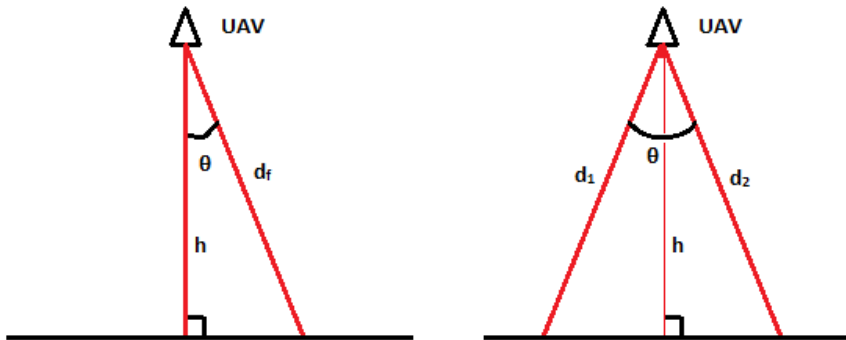


Figure 12.1: 2D scheme of two versions of array laser altimeter setup. (Left) One downward and one forward facing laser. (Right) One backward and one forward facing laser.

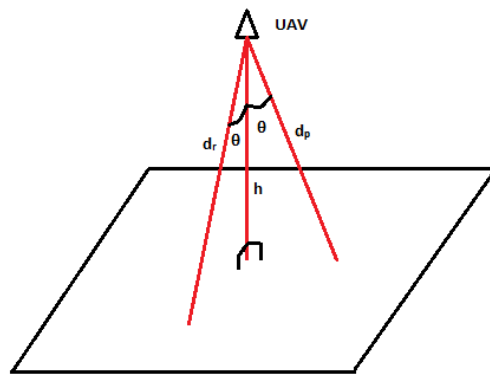


Figure 12.2: Scheme of an array of laser altimeter setup mounted on a rightward flying UAV. A 3D version of the figure 12.1 left with d_p pointing forward and d_r to the side.

12.2 Implementaion to the UAV Control System

Unmanned Aerial Vehicles requires a control system unit to process sensor data and to handle steering on the fly. Units designed for this purpose are called Flight Management Units (FMU). The FMU has built-in sensors, often motion sensors like accelerometer and gyroscopes, and can be connected to external

sensors like GPS and altimeters. It has implemented a control algorithm, which processes the sensor data and controls the motors. A common choice is the Pixhawk board [39]. The Pixhawk supports interfacing peripheral sensors through the I2C protocol. Hence, communication with the SF10 altimeters is achievable, as seen in figure 12.3 (left). I2C is a serial communication protocol developed by Philips Semiconductors, and supports multiple peripheral slave devices to communicate with the master device [50]. With a I2C splitter module multiple altimeters can be connected to the Pixhawk board.

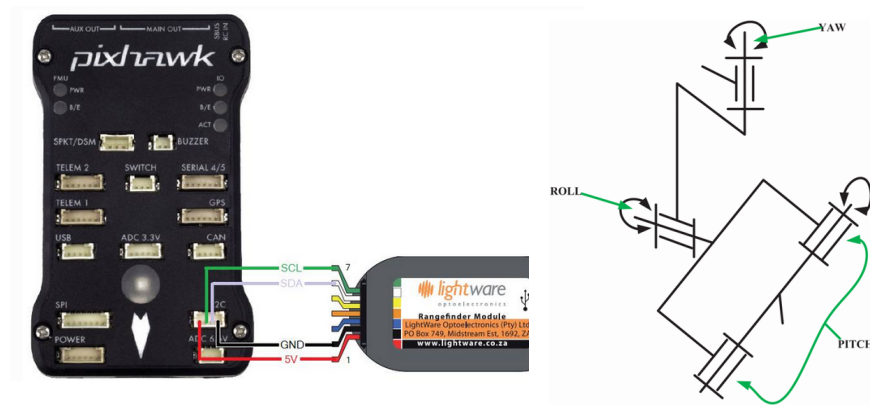


Figure 12.3: (a) Pixhawk UAV control board connected to a SF10 altimeter through I2C port [2] (b) Principle scheme of a 3 axis gimbal, reprint from [53].

As suggested by Jenssen [26], the UWibaSS radar should be mounted on a gimbal. A gimbal is a pivoted platform that can rotate around its axis to stabilize e.g. a camera, as seen in figure 12.3 (right). There are several off-the-shelf products available for mount on UAV. By help from the laser rangefinders, it should be possible to direct the UWibaSS radar beam perpendicular to the surface, independent of the orientation of the UAV. For this purpose, it is sufficient with a two axis gimbal, one axis to compensate for deviations in pitch, and one in roll.

/ 13

Discussion

This section will be a discussion of the results presented in part III, and it will be structured in a similar manner. The discussion will include an analysis of the design and execution of the experiments as well as validation of the results obtained. Then we will also look into the implications of the results and how the choice of altimeter and array setup is expected to solve the problem presented in the introduction.

General for both the stationary and scanning experiment are that they were outdoor experiments, aiming to define the performance of a rangefinder with resolution of 1 cm. Both when designing, and setting up the experiments, it was required to be careful and accurate, to not let the error sources from the experimental setup add up to more than 1 cm.

13.1 Stationary Experiment

The experiment was designed to quantify how variations in incident angle and range affect the signal strength and accuracy of the SF10 laser rangefinder, when encountering a snow surface. The scattering of NIR radiation from snow, has been studied in relation with air- and space borne remote sensing. Research emphasize that reflection coefficient is near one at 905 nm if the optical grain size is small (~ 1 mm). On the other hand, if grain size is enlarged due to metamorphosis, the reflection coefficient drops to ~ 0.7 for 10 mm grains

(see figure 4.4) at 34. The latter is unusual large grains, considering it is referred to *optical* grain size, which found is by averaging the grain size in 3D. Snow grains can under certain conditions grow to several centimeters, but then it is nearly 2D structures, which will have a small optical grain size. The scattering was expected to be diffuse, as the incident wave is likely to penetrate the surface due to the transparency of ice, but is eventually scattered back, since the number of ice/air interfaces is very large. Also, the surface roughness parameter RMS height of snow, by Rees found to be 0.5-3 cm [54], is about six orders of magnitude larger than the radiation wavelength of 0.9 μm . By Rayleigh roughness criterion, a much larger RMS height than wavelength implies diffuse scattering.

When the scattering properties were examined experimentally, we looked at the Lightware Terminal output value signal strength (SS). The SS values are presented here as the percentage of SS to precipitation particles at 0.5 m range, which was the maximum SS measured.

SS was strong over the range 0.5 - 3.5 m (see figure 9.3b). The normalized SS dropped to 93% over this range. The scattering was diffuse, as we saw from figure 9.3a that SS is reduces by 4% from 0 to 0-40° at 1 m range. Figure 6.10 compares the reduction in signal strength with accuracy. It is normalized to the same factor as the results in the stationary experiment, and thus it is valid to compare. It shows that error increases with reduction in SS. We found that expected accuracy is within ± 2 cm for SS reduced by <15% and ± 5 cm if reduced by <50% (see figure 6.10). Hence, the reduction in SS up to 3.5 m and 40° is well within the required accuracy demands for the altimeter. However, wet snow has around 5% less SS than precipitation particles, and thus, will get inaccurate at short ranges and more moderate angles.

Also, the direct range measurements by SF10 were compared to a reference distance, and the RMS error were found to be within ± 2 cm for all snow types except wet snow, that had a RMS error of 2.81 cm.

To sum up, the experimental result were consistent with the result presented in the background theory. Reflection was diffuse and strong for all types of snow, but wet snow backscattered the least amount of radiation. It is evident that the SF10 provides a robust and accurate range estimation for low altitude hovering (<5 m) and for moderate deviations in pitch and roll of the UAV.

Some of the motivation to include an independent altimeter in the UWibaSS setup, was the lack of ability to detect light dense powder snow with microwave radar. Such snow was present in the measurement campaigns of dry rounds and precipitation particles. These types had more promising results with the SF10 than wet snow. Further, the UWibaSS showed promising results in detecting

dense snow, and combining it with the SF10 will provide a complementary match.

13.2 Scanning Experiment

In this experiment, data from a SF10 altimeter was compared with corresponding data obtained by a camera filming the cross section of the snow pit while scanning a transect of 3.8 meters. Figure 10.1 shows that the AEC algorithm was accurate within ± 1 cm, which is sufficient when validating the altimeter data. The RMS error is found to be 1.56 cm when comparing SF10 to AEC data in this experiment, and figure 10.2 indicates most of this error is accumulated in the bumpy part of the slope, and that for the smooth part the accuracy within ± 1 cm.

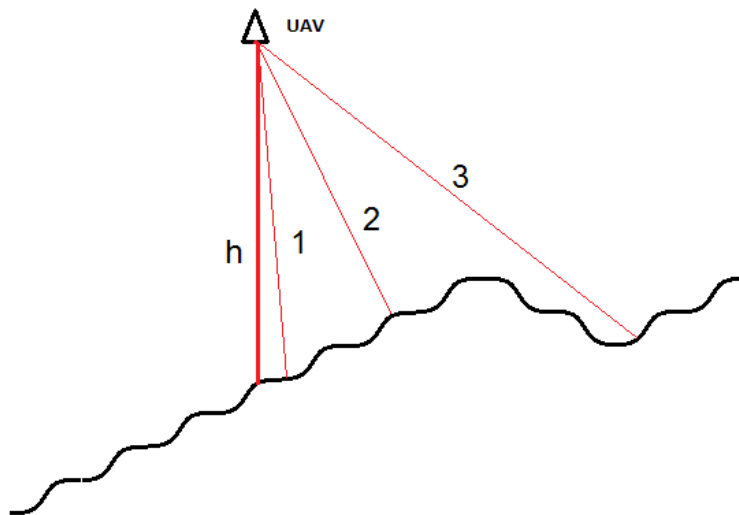


Figure 13.1: Array setup with a downward facing and three alternatives of forward facing altimeters. UAV hovering over a surface with variations on two scales.

Further, the array setup was implemented. With two altimeters, one facing 10° forwards (f), and one 10° backwards (b), the height and surface tilt was estimated. Results were acceptable (within ± 2 cm and $\pm 2^\circ$) where the surface topography was smooth, but less accurate, where the surface was more bumpy. An attempt with downward and forward directed altimeters gave significantly more accurate tilt estimation. The latter is assumed not to be a result of the setup itself, but the fact that the distance s between the points on the surface

that distance is measured to, lies closer together. The algorithm is based on a flat surface model, and s should be significantly smaller than the curvature radius of the surface, for the model to be valid.

When implementing the array setup on an UAV, the angle between the sensors must be chosen carefully. If s is too large, one may not be able to assume the surface to be flat, but if s is too small, smaller ripples or irregularities on the surface will be able to corrupt the tilt estimation. As shown in figure 13.1, a surface height can vary on several scales simultaneously. In this case it appears as forward pointing beam 1 is too close to downward beam h , and 3 is too far. By beam 2 the surface tilt angle could be resolved. The setup shown in figure 12.1 (left) and 12.2 with a $\theta = 10^\circ$ will have an $s = 35$ cm when hovering 2 m over ground. This would rule out noise from small scale roughness since RMS height typically is 0.5-3 cm [54] for snow.

13.3 Complementary Results

The experiment conducted to explore the long range abilities of the SF10, was less sophisticated than those performed in the stationary experiment. However, it proved that the SF10 can estimate altitude at least within ± 20 cm when approaching 25 m range. A more thorough experiment would probably conclude with even higher accuracy.

The RMS in the crosstalk experiment suggest that 10° is sufficient angulation between the sensor, in regards to crosstalk. It is possible to have low beam divergence in optical instruments, compared to microwave and acoustic transceivers, hence, crosstalk is easier to avoid. This is a drawback for microwave and acoustic sensors in this specific application.

13.4 Choice of Altimetric System

As it was specified in the introduction, we wanted to find an altimetric system that solved the task of robustly resolve altitude and attitude relative to a snow surface in real-time. The motivation was to be able to direct the UWibaSS radar perpendicular to the surface, and find a reference point on the top of the snowpack, which is crucial in obtaining acceptable snow stratigraphy measurements by the UWibaSS. The accuracy should be better than 5.3 cm, as this was the measured range resolution of the UWibaSS [26]. Also, power consumption, volume and weight should be kept to a minimum, due to the limitations of the UAV platform payload.

Conventional instrumentation like GPS and barometric systems were ruled out by several reasons, but first and foremost will they not provide information relative to the surface of the snowpack. Thus, we looked into active remote sensing applications, where acoustic or EM radiation are emitted from a UAV mounted sensor. The radiation interacts with the snow surface, and a fraction of it is backscattered in the direction of the UAV. The reflected radiance can be measured, and information of the distance between the UAV and the surface of the snowpack can be obtained. As we have seen in this thesis, by assuming a local flat surface, the relative angle between the UAV and the snow surface can be resolved by an array of rangefinders. On the other hand, this assumption is not necessary if a lidar is applied.

13.4.1 Lidar

Fast rotating laser rangefinder, here referred to as lidars, can be mounted on UAVs to provide estimation of the position and orientation of the UAV relative to the surrounding environment in real-time [32]. Two lidars will give a full 3D mapping, from where altitude and attitude can be resolved. The aim of our altimetric system is, however, not to provide a mapping of the surroundings, but directing the UWibaSS radar beam perpendicularly to the surface. As long as the curvature of the surface is small relative to the altitude of the UAV, the angle can be resolved by an array of not more than three altimeters, and thus a full mapping approach seem excessive for the purpose. Lidars demand motors to rotate which will increase the energy consumption significantly compared to pulsed laser rangefinders (see table 5.5 at page 44).

13.4.2 Radar Rangefinders

Altimeters based on micro or millimeter-wave radars are commonly used to increase accuracy in altitude estimations [12]. Ayan et. al applied a millimeter

wave radar on measuring height of snow with promising results for some types of snow, and it was also proposed that a millimeter wave radar would be more robust to atmospheric attenuation than optical rangefinders. As discussed in regards to the UWiBaSS radar, microwaves have a low reflection coefficient for powder snow [28, 26]. Reflection is increased going into millimeter-wave band, but is still around 0.1 at 36 GHz for dry, small grained snow [28]. Such radars would also be suspect for crosstalk with the UWiBaSS radar, as it is located nearby in the electromagnetic spectrum, which is not the case for acoustic and optical sensors. Compared to laser, the radiation pattern of micro- and millimeter-waves is harder to confine by the use of lenses, which implies that crosstalk will be a more crucial factor if an array of microwave rangefinders setup is proposed. As the wavelength is typically 2-3 orders of magnitude longer for millimeter-waves compared to optical, the latter will provide a more diffusely scattered field, and thus more robust for attitude deviations.

13.4.3 Acoustic Rangefinder

Acoustic rangefinder are in general low-cost, low power consumption and accuracy on centimeter level. Most rangefinders with range resolution of <2 cm have shorter maximum range than EM rangefinders [40]. Acoustic waves may also be interfered by turbulence from the rotors, which can increase the error compare to the ideal case. The typical wavelength of acoustic radiation is much longer than for laser rangefinders, implying that reflection at low grazing incident angles are lower. Also, beamforming is easier in the optical band.

13.4.4 Laser Rangefinder

The results of this thesis, from applying a NIR rangefinder on various types of snow, have underpinned the discussion from chapter 3 where the NIR rangefinder was found most promising. Even though wet snow is slightly darker in terms of reflection going into the NIR band, the reflection was strong and the range measurements consistent. The corresponding accuracy would likely be preserved in many cases with a millimeter-wave radar, but the low dielectric constant of powder snow would still be a concern, and we consider a NIR rangefinder as a complementary match with the UWiBaSS range finder as they are wide apart in the electromagnetic spectrum. This is an advantage both in terms of limiting crosstalk, and that different snow types are considered challenging to detect for the two bands. More precisely, light dense powder snow, which was the most prominent concern in the MW band, is the easiest to detect by a NIR rangefinder. Furthermore, the sensor is light, with low power consumption and provides a small beam divergence, making it ideal for an

array setup. This setup provides a fast way to resolve relative attitude and altitude compared to the more complicated lidar approach.

/14

Conclusions

This thesis provides a basic platform on how robust and accurate altitude and attitude estimations for an UAV hovering at low altitudes can be carried out.

Experiments with the SF10 laser altimeter on the most typical snow types was conducted, and it was clear that wet snow were significantly less reflective than other snow types. However, within the required range (<5 m) and angles ($<40^\circ$) the signal strength is expected to be over 80% for wet snow, a response that is measured to have an error of ± 2.5 cm. Direct range measurements gave average RMS error of 1.39 cm over all snow types and 2.81 cm for wet snow. This is well within the UWiBaSS microwave radar range resolution of 5.3 cm, and the SF10 laser rangefinder appears to be well suited for the purpose of estimating the distance to the top of the snow pack.

In order to estimate pitch and roll of the UAV, under the assumption that the surface is locally flat, we proposed a setup with one downward, one forward and one sideways facing altimeter simultaneously recording the distance to ground. If the surface was sufficiently flat relative to the distance between the illuminated spots on the ground, angle was estimated within $\pm 2^\circ$ and height was estimated with an RMS error off 1.57 cm. Error values were obtained by comparing height estimations by AEC algorithm, witch was assumed to be accurate at least within ± 1 cm. This implies that the array setup will resolve bot attitude and altitude within the requirements, and hence solves the task of aiding the UWiBaSS microwave radar in finding a reference point on the

top of the snow pack, as well as directing the radar beam orthogonally to the surface, while scanning over the surface.

14.1 Future Work

First and foremost, the future work will include integrating the array of SF10 altimeters with the UWibaSS radar, as discussed in chapter 12. However, there are several possibilities to further validate and develop the array of altimeters system, which will be presented below.

In order to fully validate the performance of the SF10 altimeter, it should be performed UAV flight testing. Vibrations from the UAV may have an influence on the distance read, as the range estimation is based on sequential equivalent time sampled signals. However, considering the high pulse repetition frequency (36 kHz) this should not be too damaging.

Even though range measurements are the main feature of the SF10 rangefinder, the stationary experiment showed a clear correlation between signal strength and the type of snow illuminated. Wet snow backscattered significantly less energy and could hence be strictly distinguished from the other types considered, which all could be classified as dry snow. As chapter 4 stated, the large spherical grains, such as those we found when measuring wet snow, only will develop during a wet metamorphism. Hence the SF10 have the potential to be a more integrated part of the UWibaSS system by determining if the snow pack is covered by dry or wet snow. Grain size mapping by active near-infrared sensors is a well known technique [7, 48] and is applied in estimating albedo [73] and avalanche risk [9].

Default instrumentation on many UAVs today includes GPS (speed and position), barometer (altitude), accelerometer and gyroscopes (attitude). The presented array setup will estimate the altitude and attitude of the UAV by utilizing three range measurements at one time instant, possibly after low pass filtering. None of the mentioned sensors can directly resolve the relative angle between the UAV and the ground, or find altitude within required accuracy. However, by using sensor fusion techniques (e.g. Kalman filter), one or more of the mentioned sensors can be included in the feedback system, making the system more robust, for instance if one of the SF10 altimeters fail to estimate range.

Bibliography

- [1] Ieee standard definitions of terms for antennas. *IEEE Transactions on Antennas and Propagation*, 17(3):262–269, May 1969.
- [2] Connecting sf10 to pixhawk instructions, 2017. <http://ardupilot.org/copter/docs/common-lightware-sf10-lidar.html>.
- [3] Agilent Technologies. *What is the difference between an equivalent time sampling oscilloscope and a real-time oscilloscope*, 11 2013.
- [4] Christopher Allen. Low-altitude laser altimeter to assist uav autolanding. Master’s thesis, University of Kansas, 2012.
- [5] S. Ayhan, M. Pauli, S. Scherr, B. Göttel, A. Bhutani, S. Thomas, T. Jaeschke, J. M. Panel, F. Vivier, L. Eymard, A. Weill, N. Pohl, and T. Zwick. Millimeter-wave radar sensor for snow height measurements. *IEEE Transactions on Geoscience and Remote Sensing*, 55(2):854–861, Feb 2017.
- [6] Backcountry Access (BCA). Polycarbonate crystal card, 2017. <http://backcountryaccess.com/product/polycarbonate-crystal-card/>.
- [7] Y. Buhler, L. Meier, and C. Ginzler. Potential of operational high spatial resolution near-infrared remote sensing instruments for snow surface type mapping. *IEEE Geoscience and Remote Sensing Letters*, 12(4):821–825, April 2015.
- [8] Yves Bühler. Remote sensing tools for snow and avalanche research. In *Proceedings of the 2012 International Snow Science Workshop, Anchorage, Alaska*, pages 264–268, 2012.
- [9] Y. Bühler, L. Meier, and C. Ginzler. Potential of operational high spatial resolution near-infrared remote sensing instruments for snow surface type mapping. *IEEE Geoscience and Remote Sensing Letters*, 12(4):821–825, April 2015.

- [10] A. E. Carr, L. G. Cuthbert, and A. D. Olver. Digital signal processing for target detection fmcw radar. *Communications, Radar and Signal Processing, IEE Proceedings F*, 128(5):331–336, October 1981.
- [11] A.T.C. Chang, J.L. Foster, D.K. Hall, A. Rango, and B.K. Hartline. Snow water equivalent estimation by microwave radiometry. *Cold Regions Science and Technology*, 5(3):259 – 267, 1982.
- [12] A. Cho, Y. s. Kang, B. j. Park, C. s. Yoo, and S. O. Koo. Altitude integration of radar altimeter and gps/ins for automatic takeoff and landing of a uav. In *2011 11th International Conference on Control, Automation and Systems*, pages 1429–1432, Oct 2011.
- [13] David J Daniels. *Ground penetrating radar*, volume 1. Iet, 2004.
- [14] Jeffrey S Deems, Thomas H Painter, and David C Finnegan. Lidar measurement of snow depth: a review. *Journal of Glaciology*, 59(215):467–479, 2013.
- [15] M Dumont, O Brissaud, G Picard, B Schmitt, JC Gallet, and Y Arnaud. High-accuracy measurements of snow bidirectional reflectance distribution function at visible and nir wavelengths—comparison with modelling results. *Atmos. Chem. Phys. Discuss.*, 9(5):19279–19311, 2009.
- [16] Earth and Space Research. Glossary: Definition albedo, 2017. <https://www.esr.org/outreach/glossary/albedo.html>.
- [17] Markus Eckerstorfer, Yves Bühler, Regula Frauenfelder, and Eirik Malnes. Remote sensing of snow avalanches: Recent advances, potential, and limitations. *Cold Regions Science and Technology*, 121:126 – 140, 2016.
- [18] Armstrong R.L. Durand Y. Etchevers P. Greene E. McClung D.M. Nishimura K. Satyawali P.K. Fierz, C. and S.A. Sokratov. The international classification for seasonal snow on the ground. *IHP-VII Technical Documents in Hydrology N83, IACS Contribution N1, UNESCO-IHP, Paris*, 2009.
- [19] Rafael C. Gonzalez and Richard E. Woods. *Digital Image Processing (3rd Edition)*. Prentice-Hall, Inc., Upper Saddle River, NJ, USA, 2006.
- [20] Thomas C. Grenfell and Stephen G. Warren. Representation of a non-spherical ice particle by a collection of independent spheres for scattering and absorption of radiation. *Journal of Geophysical Research: Atmospheres*, 104(D24):31697–31709, 1999.

- [21] Alfred Hanssen. Introduction to statistical signal processing and data analysis, 2003.
- [22] J. H. Ho, C. C. Cheng, N. T. Tsou, C. S. Chen, J. Shieh, C. K. Lee, and W. J. Wu. Ultrasonic transmitters far field beam pattern altering with boundary conditions design. In *2007 Sixteenth IEEE International Symposium on the Applications of Ferroelectrics*, pages 738–741, May 2007.
- [23] Wang Huining, J. Pulliainen, and M. Hallikainen. Theoretical and experimental studies of dry snow effective permittivity in the 18 to 90 ghz range. In *Microwave and Millimeter Wave Technology Proceedings, 1998. ICMMT '98. 1998 International Conference on*, pages 1006–1009, 1998.
- [24] Rockwell Laser Industires. Laser standards and classifications.
- [25] UiT The arctic University of Norway Institute of Computer Science. Weather observations.
- [26] Rolf Ole Rydeng Jenssen. Snow stratigraphy measurments with uwb radar. Master's thesis, Department of Physics and Technology, UiT The Arctic University of Norway, Norway, 2016.
- [27] H. A. Kadir and M. R. Arshad. Improved simultaneous localization and mapping (slam) algorithms for aerial vehicle under dynamic sea surface environment. In *2016 IEEE International Conference on Underwater System Technology: Theory and Applications (USYS)*, pages 61–66, Dec 2016.
- [28] D. H. Kang, A. P. Barros, and E. J. Kim. Evaluating multispectral snowpack reflectivity with changing snow correlation lengths. *IEEE Transactions on Geoscience and Remote Sensing*, 54(12):7378–7384, Dec 2016.
- [29] Nicholas P. Klingaman, Brian Hanson, and Daniel J. Leathers. A teleconnection between forced great plains snow cover and european winter climate. *Journal of Climate*, 21(11):2466–2483, 2008.
- [30] A. A. Kokhanovsky, T. Aoki, A. Hachikubo, M. Hori, and E. P. Zege. Reflective properties of natural snow: approximate asymptotic theory versus in situ measurements. *IEEE Transactions on Geoscience and Remote Sensing*, 43(7):1529–1535, July 2005.
- [31] Hans Koren. Snow grain size from satellite images. *SAMBA/31/09, Norsk Regnesentral*, 2009.
- [32] R. Li, J. Liu, L. Zhang, and Y. Hang. Lidar/mems imu integrated navigation

- (slam) method for a small uav in indoor environments. In *2014 DGON Inertial Sensors and Systems (ISS)*, pages 1–15, Sept 2014.
- [33] Wei Li, Knut Starnes, Hans Eide, and Robert Spurr. Bidirectional reflectance distribution function of snow: corrections for the lambertian assumption in remote sensing applications. *Optical Engineering*, 46(6):066201–066201–9, 2007.
- [34] LightWare Oproelectronics Ltd. *SF 10 Laser Altimeter Product Manual*, 9 2015. Rev 8.
- [35] Christian Maätzler. Relation between grain-size and correlation length of snow. *Journal of Glaciology*, 48(162):461–466, 2002.
- [36] MaxBotix Inc. *LV-MaxSonar-EZ Series High Performance Sonar Range Finder*, 2006.
- [37] J.H. McClellan, R.W. Schafer, and M.A. Yoder. *Signal Processing First*. Number v. 1 in *Signal Processing First*. Pearson/Prentice Hall, 2003.
- [38] D. McClung and P.A. Schaerer. *The Avalanche Handbook*. Mountaineers Bks. Mountaineers Books, 2006.
- [39] L. Meier, D. Honegger, and M. Pollefeys. PX4: A node-based multithreaded open source robotics framework for deeply embedded platforms. In *Robotics and Automation (ICRA), 2015 IEEE International Conference on*, may 2015.
- [40] P. Misra, S. S. Kanhere, S. Jha, and W. Hu. Sparse representation based acoustic rangefinders: from sensor platforms to mobile devices. *IEEE Communications Magazine*, 53(1):249–257, January 2015.
- [41] MTI Instruments. *Microtrak 3 Laser Triangulation Sensor*, 10 2013. Rev. 1.3.
- [42] A. Mugnai and W. J. Wiscombe. Scattering of radiation by moderately nonspherical particles. *Journal of the Atmospheric Sciences*, 37(6):1291–1307, 1980.
- [43] K Muljowidodo and A Budiyono. Design and development of micro aerial vehicle at itb. In *International Conference on Technology Fusion, Seoul, Korea*, pages 17–19, 2006.
- [44] M Naboulsi, H Sizun, and F Fornel. Propagation of optical and infrared

- waves in the atmosphere. *Proceedings of the union radio scientifique internationale*, 2005.
- [45] A. Natraj, P. Sturm, C. Demonceaux, and P. Vasseur. A geometrical approach for vision based attitude and altitude estimation for uavs in dark environments. In *2012 IEEE/RSJ International Conference on Intelligent Robots and Systems*, pages 4565–4570, Oct 2012.
- [46] R. Nebuloni and C. Capsoni. Laser attenuation by falling snow. In *2008 6th International Symposium on Communication Systems, Networks and Digital Signal Processing*, pages 265–269, July 2008.
- [47] FE Nicodemus, JC Richmond, JJ Hsia, IW Ginsberg, and T Limperis. Geometrical considerations and nomenclature for reflectance, natl. *Bur. Stand. Rep., NBS MN-160*, 1(2), 1977.
- [48] A. W. Nolin. Mapping snow grain size on the ice sheets with a laser altimeter. In *Geoscience and Remote Sensing Symposium Proceedings, 1998. IGARSS '98. 1998 IEEE International*, volume 4, pages 2264–2266 vol.4, Jul 1998.
- [49] Government of Camera. Meterological glossary.
- [50] Jivan Parab, Santosh A. Shinde, Vinod G Shelake, Rajanish K. Kamat, and Gourish M. Naik. *Practical Aspects of Embedded System Design using Microcontrollers*. Springer Netherlands, 2008.
- [51] Nicolas Pinel and Christophe Bourlier. *Electromagnetic Wave Scattering from Random Rough Surfaces*. John Wiley and Sons, Inc., 2013.
- [52] David M Pozar. *Microwave engineering; 3rd ed.* Wiley, Hoboken, NJ, 2005.
- [53] R. J. Rajesh and P. Kavitha. Camera gimbal stabilization using conventional pid controller and evolutionary algorithms. In *2015 International Conference on Computer, Communication and Control (IC4)*, pages 1–6, Sept 2015.
- [54] W.G. Rees. *Remote Sensing of Snow and Ice*. CRC Press, 2005.
- [55] William Gareth Rees. *Physical principles of remote sensing*. Cambridge University Press, 2013.
- [56] RoboPeak. *RPLIDAR, Low Cost 360 degree 2D laser Scanner System*, 2014.

- [57] A Rognesa, R Solberga, Jostein Amlien, Hans Koren, Line Eikvil, E Malnesb, R Storvoldb, I Lauknesb, and Tom Andersen. Satellite based snow monitoring for hydropower production and trade in norway—results versus operational needs. 2005.
- [58] Roke Manor Research Ltd. *Miniature Radar Altimeter*, 2009.
- [59] H. Rott. The analysis of backscattering properties from sar data of mountain regions. *IEEE Journal of Oceanic Engineering*, 9(5):347–355, Dec 1984.
- [60] H. Rott, R. E. Davis, and J. Dozier. Polarimetric and multifrequency sar signatures of wet snow. In *Geoscience and Remote Sensing Symposium, 1992. IGARSS '92. International*, volume 2, pages 1658–1660, May 1992.
- [61] Alexandre Roy, Alain Royer, and Richard Turcotte. Improvement of spring-time streamflow simulations in a boreal environment by incorporating snow-covered area derived from remote sensing data. *Journal of Hydrology*, 390(1–2):35 – 44, 2010.
- [62] Eckerstorfer M. Vickers H . Høgda K. Malnes E. Jacobsen S.K. Rydeng Jenssen, R.O. Drone-based uwb radar to measure snow layering in avalanche starting zones. In *International Snow Science Workshop, Breckenridge, Colorado*, 2016.
- [63] M.N.O. Sadiku. *Elements of electromagnetics*. The Oxford Series in Electrical and Computer Engineering Series. Oxford University Press, Incorporated, 2007.
- [64] A Schaffhauser, M Adams, R Fromm, P Jörg, G Luzi, L Noferini, and R Sailer. Remote sensing based retrieval of snow cover properties. *Cold Regions Science and Technology*, 54(3):164–175, 2008.
- [65] H. K. Schoenwetter. Recent developments in digital oscilloscopes. In *6th IEEE Conference Record., Instrumentation and Measurement Technology Conference*, pages 154–155, Apr 1989.
- [66] J.R. Schott. *Remote Sensing: The Image Chain Approach*.
- [67] Jürg Schweizer. Snow avalanche formation and dynamics, 2008.
- [68] JR Shell. Bidirectional reflectance: An overview with remote sensing applications & measurement recommendations. *Rochester NY*, 2004.

- [69] M. Shokr and N. Sinha. *Sea Ice: Physics and Remote Sensing*. Geophysical Monograph Series. Wiley, 2015.
- [70] B. Tremper. *Staying Alive in Avalanche Terrain*. Mountaineers Bks. Mountaineers Books, 2001.
- [71] L. Tsang and J.A. Kong. *Scattering of Electromagnetic Waves, Advanced Topics*. Scattering of Electromagnetic Waves. Wiley, 2004.
- [72] Steve Vavrus. The role of terrestrial snow cover in the climate system. *Climate Dynamics*, 29(1):73–88, 2007.
- [73] Warren J. Wiscombe and Stephen G. Warren. A model for the spectral albedo of snow. i: Pure snow. *Journal of the Atmospheric Sciences*, 37(12):2712–2733, 1980.
- [74] Hongsheng Zhang, Yuanzhi Zhang, and Hui Lin. A comparison study of impervious surfaces estimation using optical and sar remote sensing images. *International Journal of Applied Earth Observation and Geoinformation*, 18:148 – 156, 2012.
- [75] W. Zhu, Y. Dong, G. Wang, Z. Qiao, and F. Gao. High-precision barometric altitude measurement method and technology. In *2013 IEEE International Conference on Information and Automation (ICIA)*, pages 430–435, Aug 2013.